REPORT DOCUMENTATION PAGE

Form Approved
OMB No. 0704-0188

1. REPORT DATE *(DD-MM-YYYY)*	2. REPORT TYPE	3. DATES COVERED *(From - To)*
05/09/2013	Final report	05/06/2007-12/31/2012

4. TITLE AND SUBTITLE
Proposal for research on high-brightness cathodes for high-power free-electron lasers

5a. CONTRACT NUMBER

5b. GRANT NUMBER
N00014-07-1-1037

5c. PROGRAM ELEMENT NUMBER

6. AUTHOR(S)
Brau, Charles A.

5d. PROJECT NUMBER

5e. TASK NUMBER

5f. WORK UNIT NUMBER

7. PERFORMING ORGANIZATION NAME(S) AND ADDRESS(ES)
Vanderbilt University
Division of Sponsored Research
Baker Building Suite 937
110 21st Avenue South, Nashville, TN 37203

8. PERFORMING ORGANIZATION REPORT NUMBER

9. SPONSORING/MONITORING AGENCY NAME(S) AND ADDRESS(ES)
Sarwat Chappell
Office of Naval Research
875 North Randolph Street
Arlington, VA 22203-1995

10. SPONSOR/MONITOR'S ACRONYM(S)
ONR

11. SPONSOR/MONITOR'S REPORT NUMBER(S)

12. DISTRIBUTION/AVAILABILITY STATEMENT

13. SUPPLEMENTARY NOTES

14. ABSTRACT
It is widely recognized that the development of high-power free-electron lasers will depend critically on advances in optical resonators and electron injectors. In the last few years, there have been major improvements in optical coatings, cooled mirrors and alignment systems. Likewise, electron injectors have seen enormous improvements since the beginning of the FEL program.

15. SUBJECT TERMS
Field emission; cathodes; electron guns; free-electron lasers

16. SECURITY CLASSIFICATION OF:			17. LIMITATION OF ABSTRACT	18. NUMBER OF PAGES	19a. NAME OF RESPONSIBLE PERSON
a. REPORT	b. ABSTRACT	c. THIS PAGE			John Childress
					19b. TELEPHONE NUMBER *(Include area code)*
U	U	U	UU	29	615-322-3977

Vanderbilt University JTO/ONR HEL MRI

Final Report

Project Title: "Proposal for research on high-brightness cathodes for high-power free-electron lasers" (FEL)

Point of Contact: Professor Charles Brau

1. Introduction

It is widely recognized that the development of high-power free-electron lasers will depend critically on advances in optical resonators and electron injectors. In the last few years, there have been major improvements in optical coatings, cooled mirrors and alignment systems. Likewise, electron injectors have seen enormous improvements since the beginning of the FEL program.

The so-called "normalized brightness" of an electron beam is a measure of the beam quality, the degree to which high current can be focused into a small spot with good collimation. The normalized brightness of various electron-beam sources is summarized in Figure 1.1 [i]. As shown there, the peak current of various sources spans nine orders of magnitude, while the peak brightness spans more than eight orders of magnitude! At the bottom of the graph we find the dc photocathode gun used in the high-power FEL experiments at Jefferson Laboratory [ii]. Higher brightness and current are provided by rf photoelectric injectors, which are currently the injectors of choice for high-power, short-wavelength FELs. High-average-power FELs became a realistic possibility because of the development of the room-temperature rf photoinjector. The key to the high brightness and current of the rf photoelectric injector is the very high field at the cathode in an rf cavity and the fact that the emission from a photocathode can be timed to the optimum phase of the rf cycle. Emittance growth due to the time-varying rf fields has been successfully addressed by "emittance compensation." Nevertheless, as indicated in Figure 1.2 [iii], the most durable photocathodes are the least efficient, and the most efficient photocathode material available at the present time is probably too slow for use in an rf gun. In the last few years very little progress has been made on this problem. Some progress is being made in dispenser photocathodes and diamond amplifiers, but the outcome is uncertain. To the fragility of the photocathode must be added the complexity of the drive laser system. Given a dependable quantum efficiency on the order of a few percent at a photon energy of 3 eV, the average laser power required to produce an e-beam current of 1 A is about 100 W in the near ultraviolet. To this

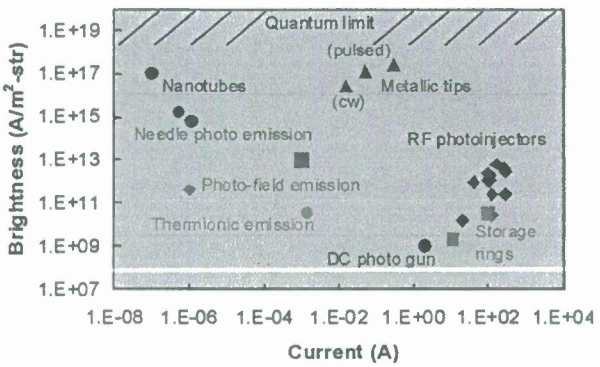

Figure 1.1: Current and normalized transverse brightness of various electron sources.

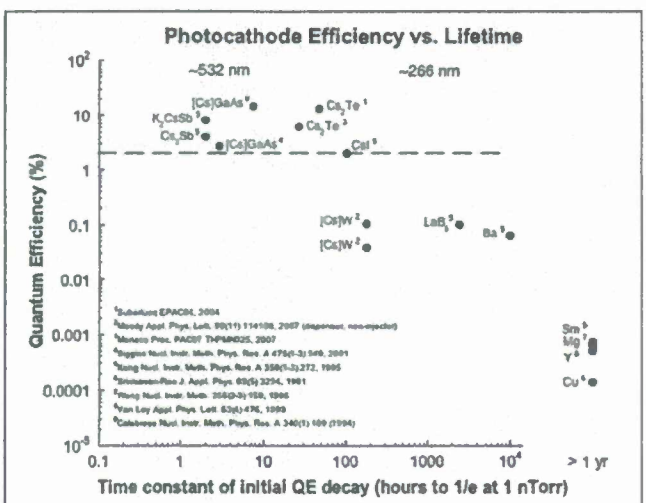

Figure 1.2: Lifetime and efficiency of available electron sources.

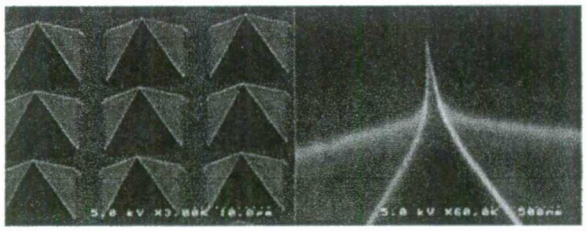

Figure 1.3: SEM micrograph of diamond-pyramid field emitters showing an array and a close-up of a single tip.

must be added the demands of picosecond mode-locked operation, and longitudinal and transverse pulse shaping to optimize the e-beam brightness. These requirements will be difficult to meet in a reliable system. It is very important to find an alternative to laser photocathodes.

Two possible alternatives to photocathodes have emerged. The first, and the subject of this report, is the diamond field-emitter array (DFEA). The second is the gridded thermionic cathode, based on the development of gridded cathodes for high-power microwave tubes. Although thermionic cathodes themselves are known to be rugged, the beam properties of emittance and pulse length have never been measured in an rf gun. There is concern that the grid fields will disturb the emittance and the grid capacitance will compromise emission uniformity in short pulses. It is important, therefore, to continue the successful development of DFEA cathodes as an alternative to photocathodes.

The history of field-emitter arrays (FEAs) begins with the work of Spindt in the 1960s [iv]. Using microelectronic lithography techniques available at that time, Spindt was able to fabricate arrays of cone-shaped metallic tips with integrated gate electrodes. The Spindt cathode has demonstrated the capability for high current density operation with reasonable beam quality [v,vi]. However, stable emission requires UHV conditions, and reliable operation of individual arrays larger than 1 mm^2 has been difficult to achieve [vii]. Diamond field-emitter arrays (DFEAs) have several advantages over Spindt cathodes. Diamond is hard, chemically stable, and has excellent thermal conductivity. At Vanderbilt we have developed the technology (VU patent # 6132278) to fabricate large arrays of very sharp diamond pyramids [viii,ix]. The pyramids are formed with a mold-transfer process in which pyramidal molds are etched into a silicon substrate and filled with chemical-vapor deposited (CVD) diamond. The diamond is then brazed to a molybdenum substrate and the silicon mold is etched away. To form sharp tips, the silicon mold is oxidized before the diamond is deposited. This leaves a cusp at the bottom of the mold that is filled by the diamond to form a tip with a radius of curvature on the order of 5-10 nm. A completed DFEA with detail of an emitter tip is shown in Figure 1.3.

Previously, we successfully addressed the three most important issues for field-emitter arrays, namely uniformity of emission, current density, and emittance. To condition the arrays for uniform emission, we developed a process called Vacuum Thermal-Field Emission (VTFE) [x]. The apparatus is shown in Figure 1.4. In this process we use a combination of high temperature (up to 500C) and high current to effect a combination of morphological and chemical changes in the surface of the tips. For the highest current densities it is necessary to use pulsed conditioning [xi]. If the beam is left on for more than a couple of microseconds, the intensity is high enough to damage the anode, causing material to sputter back on the cathode. This also establishes the limits to which we have been able

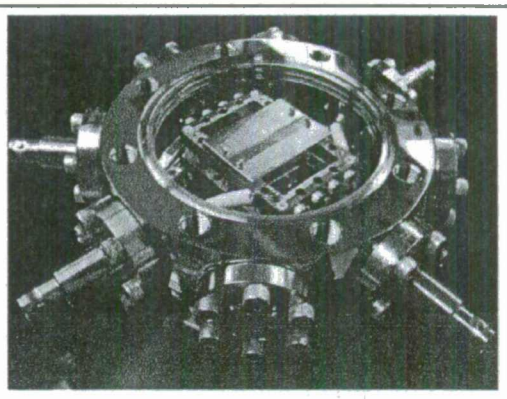

Figure 1.4: Apparatus used to condition and test DFEAs .

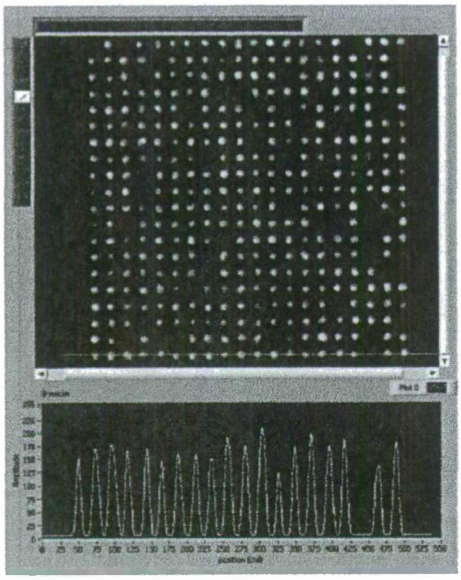

Figure 1.5: Example of uniform emission from a DFEA .

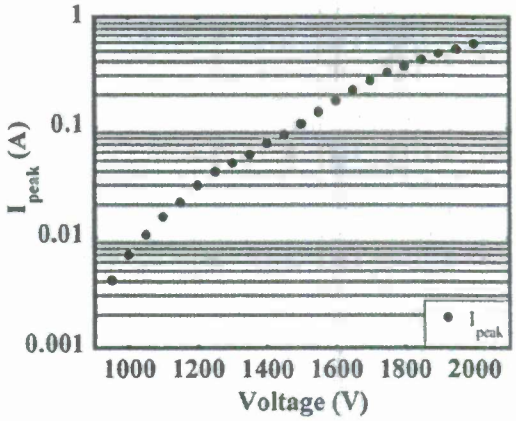

Figure 1.6: Total current obtained from a 224 by 448 array.

to test the cathodes. An example of the uniformity of conditioning is shown in Figure 1.5, where 90% of the tips emit with a uniformity of +/-10%.

Using the test apparatus shown in Figure 1. 4 and a 224 by 224 array of 10-micron tips with a pitch of 14 microns, we previously achieved current densities as high as 30 A/cm^2 in microsecond pulses, limited by damage to the anode. Using a 224 by 448 array, we obtained the data shown in Figure 1.6. The highest current obtained, 600 mA, corresponds to 12 μA/tip. This was limited by the power supply.

We also measured in detail the properties of the electron beam. In the first experiment, we measured the emittance of the beam using a standard pepper-pot technique. The pepper-pot mask was formed by ps-laser machining 50-micron holes in a stainless steel foil. From the spots on the fluorescent screen it is found that after correcting for the focusing by the pepperpot hole the beam divergence is 38 milliradians at 1.3 kV. This is in excellent agreement with the 40 milliradians predicted by numerical simulations of the beam. The corresponding rms normalized emittance for a uniformly emitting 1-cm cathode is 10 μm. This satisfies the requirement for a 1-MW near-infrared FEL.

In a separate set of experiments we measured the energy spectrum of the electrons field-emitted from a diamond tip using a retarding-potential analyzer. This has revealed enormous information about the physics of emission from diamond field emitters. The results show that the emission from a diamond tip is dominated by resonant tunneling through individual molecules adsorbed on the surface. When we examine the total current from a single tip, we observe the step-wise fluctuations caused by the arrival, departure, and diffusion of adsorbed molecules on the surface of the tip, as shown in Figure 1.7 [x].

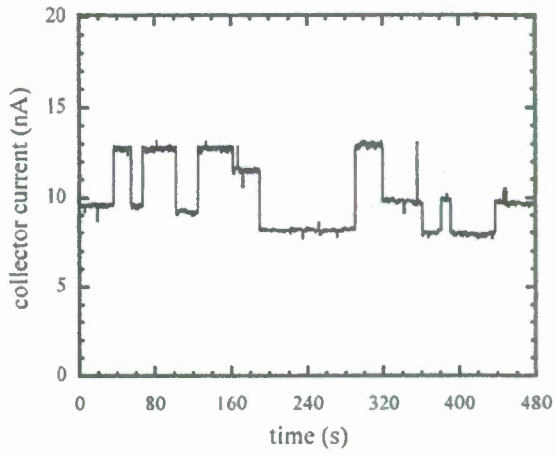

Figure 1.7: Fluctuations in the current from a single diamond-pyramid field emitter.

Finally, there is the issue of integrating the FEA into the injector. To avoid deterioration of the beam due to space charge, it is important to accelerate the beam quickly in a strong electric field. This is most reliably accomplished in rf cavities. To avoid expanding the energy spread and emittance of the beam, it is necessary to inject the beam into the rf cavity in a short pulse properly timed to the phase of the fields. Historically, this has been done by illuminating a photocathode in the rf cavity with a mode-locked laser synchronized to the rf cycle. Field-emission cathodes must be controlled differently. By their nature, field emitters emit very strongly at the peak field on the cathode, which does not correspond to the phase required for optimum acceleration. Due to the transit time of the rf cavity, electrons must be emitted from the cathode before the field in the cavity reaches its peak.

We have identified several possible solutions to this problem. Lewellen has pointed out the use of multiple-frequency rf cavities [xii]. By using carefully designed rf cavities resonant at the first and third harmonics, it is possible to have the field at the cathode peak at a different time than the field in the main body of the cavity. In this case it might even be possible to control the timing of the emission without using the control gates in the FEA. Alternatively, the FEA can be placed in the back face of the rf cavity with sufficient gate control to time the emission to the correct rf phase. Since the gates are driven by relatively low-level signals, on the order of hundreds of volts or less, rf drive of the FEA is possible using ordinary coaxial feeds. Other configurations, including combinations of these ideas, are possible. For example, a third-harmonic field could be used to shorten the emission pulse.

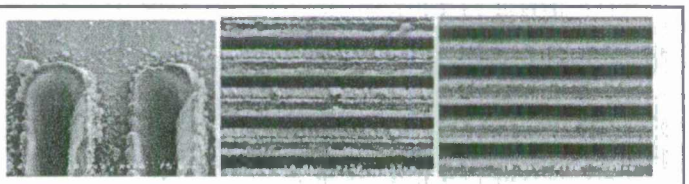

Figure 1.8: Laser machining using (left) nanosecond, (center) picosecond, and (right) femtosecond laser pulses.

Finally, with a view toward installing and testing the arrays in actual guns, we have developed laser machining and alignment techniques for cutting the cathodes to adapt them to actual gun geometries. We have tested machining using nanosecond, picosecond, and femtosecond laser pulses. Some results are shown in Figure 1.8. The nanosecond tests were carried out at Tullahoma and produced the poorest results with the most collateral damage. The picoseconds and femtosecond tests were done at Vanderbilt. Femtosecond pulses were the most successful and produced the clean cuts shown in Figure 1.8. In addition, since the substrate is brazed on the back of the cathode before the mold is removed, we had to develop techniques for the "blind" alignment of the substrate on the cathode by adding fiducial markers to the mask used to etch the mold before diamond deposition. An example of a cathode successfully machined using these procedures is shown Figure 1.9.

Figure 1.9: DFEA cathode laser-machined to fit a 6-mm Mo substrate .

Besides the ungated arrays described above, we have begun the development of gated arrays. Relative to ungated arrays, these have two advantages. In the first place, they can be operated with lower external fields, since the control gate can be used to increase the field at the tips. In the second place, the gate can be used to control both the level and the timing of the emission from the cathode. In this way the field in the gun can be separated from the field needed for emission, and the timing of the emission can be adjusted to the optimum phase to preserve

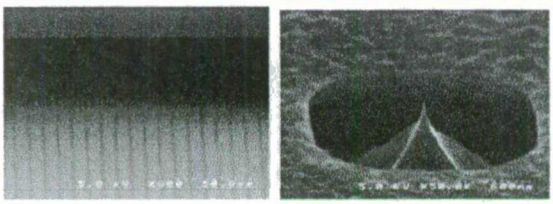

Figure 1.10: SEM micrograph of an array of gated diamond field emitters with a detail of one tip.

the emittance and energy spread. An example of a gated array is shown in Figure 1.10. The gate is formed by etching the mold just enough to leave the tips exposed. The oxide used to sharpen the tips is etched back just enough to expose the tip itself; the remaining oxide layer, about 1 micron thick, forms the insulation between the cathode and the gate.

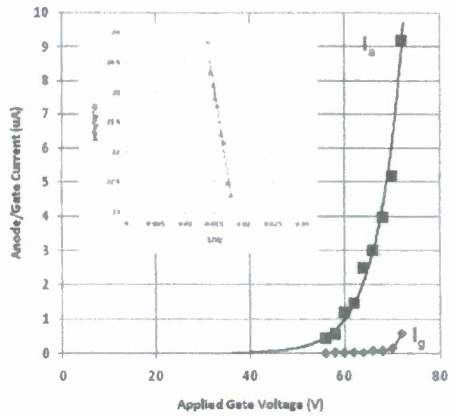

Field emission characteristics of 5x5-p4 of 2GDMA-2

Figure 1.11: Electrical performance of a gated DFEA.

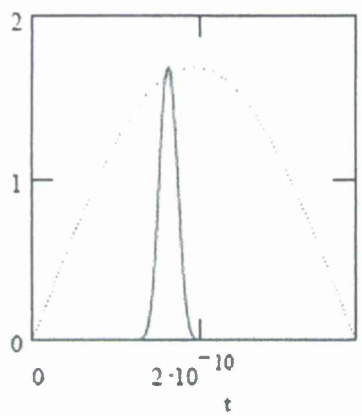

Figure 1.12: Current pulse (red curve, arbitrary units) from a gated DFEA biased at the third harmonic of the cavity rf field (blue curve, arbitrary units) versus time (s).

The ability of the gate to control the current is illustrated in Figure 1.11. As shown there, the gate operates at relatively low voltages, typically less than +/- 70 V, depending on the geometry of the gate. At voltages less than about 10 V the current is completely cut off. From 10 to 70 V the current increases. Above 70 V, the gate current increases due to interception of electrons attracted to the gate. This limits the gate voltage since excess gate current can damage the gate and lead to failure of the cathode. These performance parameters can be adjusted by altering the cathode-gate geometry to optimize the performance when the cathode is used in an rf electron gun. An example of the performance that might be expected is shown in Figure 1.12, where the gate is driven at the third harmonic of the rf cavity to obtain a 10-degree pulse advanced 15 degrees ahead of the peak of the cavity field.

The research discussed in this report focuses on three broad areas. First, we have continued the development of ungated DFEAs. Second, we have developed gated DFEAs using a new process, called the "volcano" process. Third, we have begun testing DFEA cathodes in rf guns

2. Ungated arrays

a. Fabrication

All diamond fabrication has now been transferred to the VINSE facilities. The move to VINSE has resulted in increased production efficiencies and significant enhancement of our fabrication capabilities, including different oxidation and mold conditioning techniques, the production of all metal and diamond/metal composite emitters, and the development of direct-deposition and large-area brazing techniques. Additionally the move has made possible the development of volcano-style gated-emitter arrays.

Lithography and mold etching

Our lithography procedures have produced patterned hole arrays that are uniform in shape and size over multi-centimeter length scales. Previously we produced 7-μm pitch arrays with a 5-μm emitter base width. We now fabricate 4-μm pitch, 2-μm base width arrays for higher current density, and sparse arrays with >100-μm pitch for the isolation of individual beamlets and the determination of maximum per-tip current. Figure 2.1 shows a 4-μm pitch mold prior to chrome mask removal and oxidation. We have also demonstrated that the reliable fabrication of quad-tip emitters is possible as a method of increasing current density in exchange for higher turn-on field.

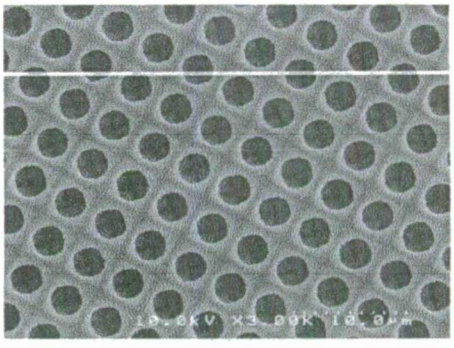

Fig. 2.1: 4-μm pitch mold with 2-μm pyramid base width. The mold is shown prior to chrome mask removal or oxidation.

Oxidation and deposition

Diamond seeding: We now utilize sonication in a diamond-nanoparticle slurry, and bias-enhanced nucleation (BEN) to encourage the conformal growth of high-quality nanodiamond films in the cathode molds. We have considered the effects of variable exposure time for BEN as seen in Figure 2.2. It is observed that BEN overexposure produces a high quality diamond film but damages the oxide in the pyramidal mold leading to undesirable surface roughness.

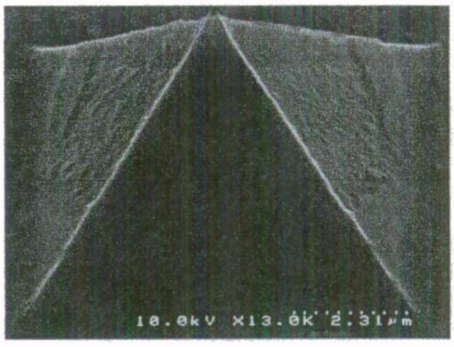

Fig. 2.2: BEN overexposure of the pyramidal mold causes damage to the sharpening oxide. The roughened surface of this pyramid is the result of 60 min of BEN rather than the usual 30 min.

Double and thick oxidation studies: We have applied our previously developed wet oxidation capability to produce oxides that are up to 2 microns in thickness. This has

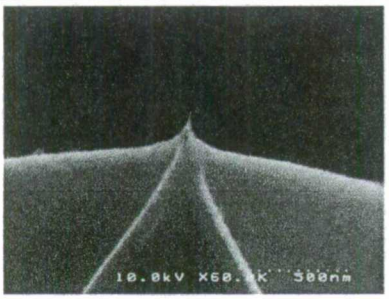

Figure 2.3: Emitter-tip detail for a cathode fabricated using (0.5 μm, 1.0 μm) double oxidation.

allowed us to experiment with double oxidation of molds whereby we improve a variety of properties of the molds and the resulting diamond tips. The double oxidation process is accomplished by first growing an oxide layer on the etched silicon mold that is on the order of 0.5 microns thick. Due to internal stresses in the mold the oxide grows more quickly on large flat surfaces than it does near cusps and corners. We use a buffered oxide etch to remove the initial oxidation, resulting in slight rounding of the mold corners. Because of this rounding the subsequent oxidation, which is typically between 1 and 2 microns thick, does not produce the sharp edges that are common in single oxidation processing. Additionally, the nanotip at the end of the pyramid is sharp but has a lower aspect ratio than is typically obtained with single oxidation, as shown in Figure 2.3. It is known that these emitters condition by thermal assisted field evaporation of the nanotip as it is processed at microamp per-tip currents. This evaporation should continue, with the tip shortening and the radius increasing, until the tip is thermally stable at that particular applied field. Tips produced with double oxidation should require the evaporation of less material to achieve this conditioned state. Furthermore, the more rapid tapering of the double oxidation molds may result in more uniform and more complete filling of the mold with diamond. If the first oxide is too thick relative to the second, then tips such as those seen in Figure 2.4 are produced. Although the edges are significantly rounded, the mold is insufficiently sharp to produce high aspect ratio tips required for emission at convenient electric fields. Figure 2.5 shows the results of a 2-μm thick single oxidation with 2-μm base pyramids. While sharp tips are produced with good yield, limitations of the lithography procedure result in many failed double tips.

Quad-tip emitters: If the KOH etching of the silicon mold is terminated prior to completion of the pyramid, then a small square flat can be left at the tip of the mold. A sufficiently thick single oxidation will result in four sharp nanotips as seen in Figure 2.6. This structure obviously has the advantage of more emitters for the same array pitch, however this comes at the cost of a higher required operating field and increased divergence of the beam from the array. For single tip emitters, if a nanotip is not well formed then the area of that entire pyramid is wasted, whereas for a quad-tip emitter there is a level of redundancy.

Molybdenum and diamond/molybdenum composite emitters: We have investigated the production of molybdenum and diamond/molybdenum composite emitters with

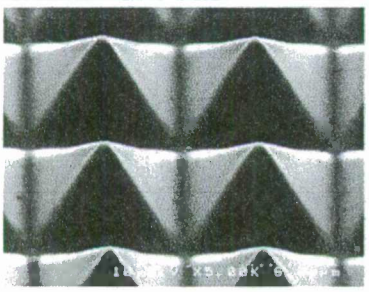

Figure 2.4: DFEA resulting from the use of (1 □m, 1□m) double oxidation.

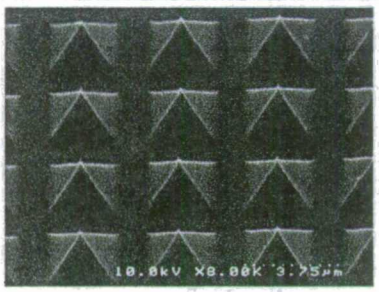

Figure 2.5: 2-μm pyramids produced with a 2-μm single oxidation

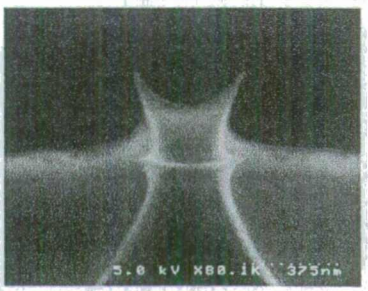

Figure 2.6: Quad tip emitter produced using a 2-μm single oxidation. The flat at the end of the pyramidal mold was on the order of 0.5 μm

the hope of providing points of comparison for the emission performance of the all-diamond structures. Thus far the molybdenum sputter source in the Angstrom deposition system has not been successful in filling the nanotip part of the mold. We have succeeded in depositing a conformal nanodiamond layer, as usual, and then backfilling with molybdenum instead of microdiamond. These structures may make for interesting comparisons to the all diamond structures especially in the context of electrical conductivity.

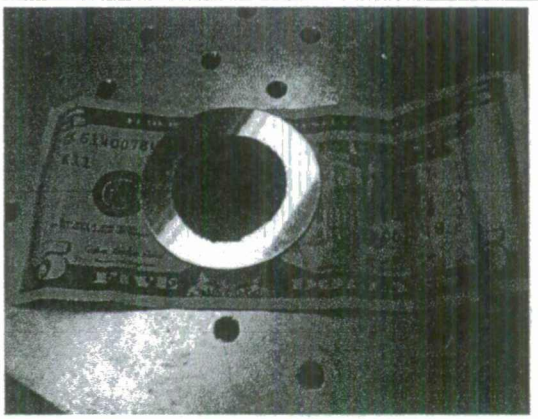

Figure 2.7: 33-mm diameter DFEA brazed to a 50-mm diameter molybdenum substrate. The cathode surface is very flat and without significant defect.

Brazing

We have assembled a new high-vacuum brazing apparatus that allows the application of temperatures up to 1100 C and substrate diameters up to 3 inches. Additionally we are able to braze up to six smaller cathodes on 19-mm substrates simultaneously, greatly increasing turn-around rate and reducing the user load on our primary testing apparatus, which was previously utilized for brazing operations. Figure 2.7 shows the first large cathode that we attempted to braze. The molybdenum substrate is 50 mm in diameter and the diamond cathode has a diameter of 33 mm. After removal of the silicon mold the 5-micron diamond film was found to be extremely flat and without any significant defect. In an important innovation in our brazing capability, we have successfully deposited braze alloy heterostructures directly on the polished substrate. The braze layer, deposited by thermal and electron beam evaporation, is approximately 8-10 microns thick and is ordered as Ag/Cu/Tl/Cu/Ag. The enhanced thermal contact with the substrate has resulted in lower, more consistent braze temperatures, better self-selection of the cathode area, fewer edge defects, and the complete elimination of braze material flow out from under the cathode area.

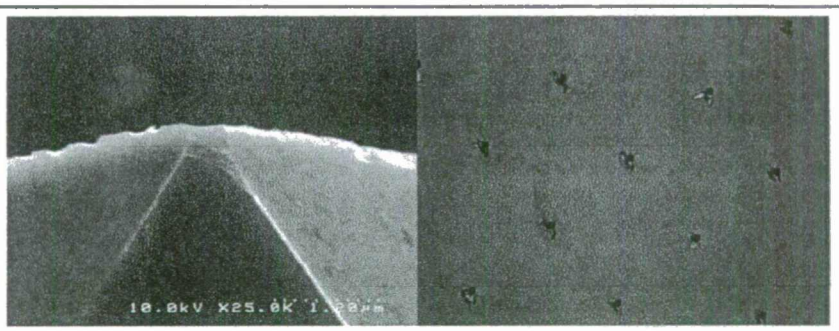

Figure 2.8: Self-delaminated mold (left: optical microscope image, SiO_2 surface and each dot is a pyramidal mold of 20 micron base), and diamond pyramid (right) SEM image, apex was broken).

We suffered from self-delaminating of mold and diamond interface during an early stage of mold removal for sparse arrays. We think the thermal expansion coefficient mismatch between mold SiO_2 and diamond structure was the major cause. Figure 2.8 shows an example of a delaminated sparse array at early stage of the mold removal step. To improve the heat distribution uniformity during brazing step, we introduced heat shields on top of our brazing apparatus. Fig. 2.9 shows a schematic of the new apparatus. Two layers of thin stainless steel disks can reduce the peak temperature for brazing and slow down the cooling to prevent heat shock in the sample. With the new brazing set-up, we succeeded in

making sparse arrays with 20-micron base pyramids.

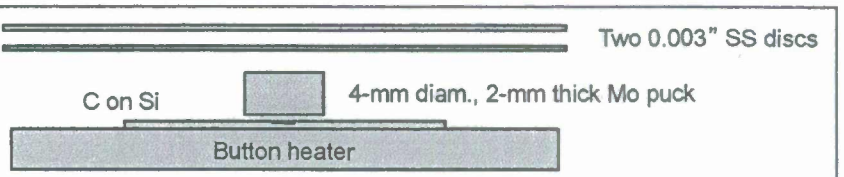

Figure 2.9: Improved brazing apparatus and set-up for 4mm diameter Mo puck. Radiation shields on top of previous set-up enhance uniformity of heat spread surrounded by molds and Mo substrate, and reduce cooling rate after brazing.

We installed a new 4" quartz tube furnace in the VINSE clean room and used it for mold oxidation and annealing steps. This furnace has multi-purpose set-ups from simple oxidation to low-pressure CVD. The oxygen gas delivery line is isolated by a three-way valve (left) with flammable gases for LPCVD (Figure 2.10 (left)). Oxidation is used for the mold sharpening step, and low-pressure CVD is for various annealing steps including hydrogenation.

In order to verify and measure LPCVD performance, we tested CVD graphene growth on a 25-μm thick copper foil with around 2" diameter area. Figure 2.11 shows a transferred single layer graphene film on

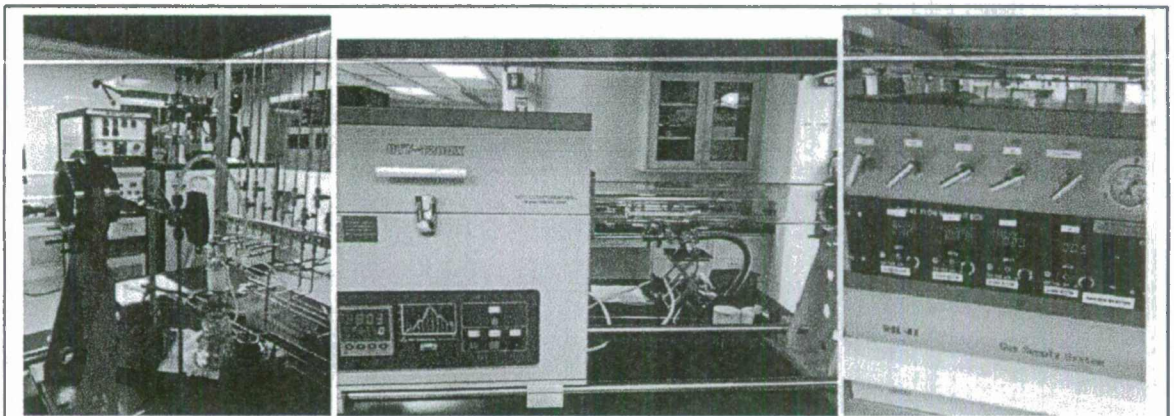

Figure 2.10: 4" quartz tube furnace (oxidation/LPCVD). Gas delivery network (left), sliding furnace and quartz tube (center), and gas mixing box and flow controller (right).

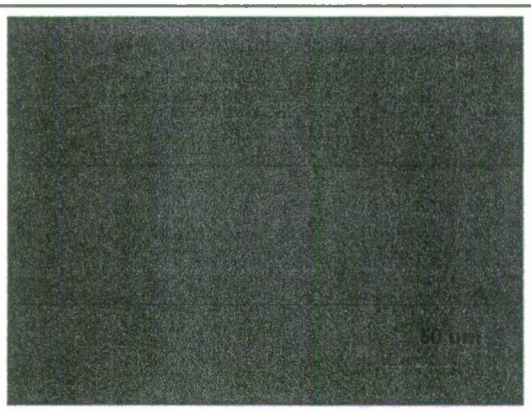

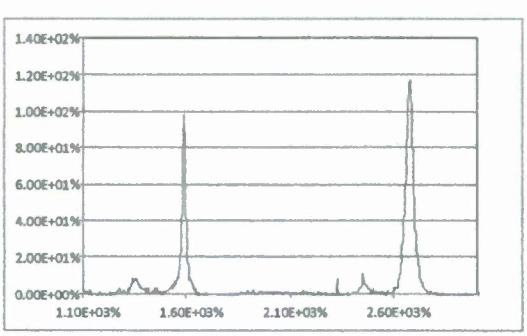

Figure 2.11: Single-layer graphene transferred on 300 nm thick SiO_2 on silicon wafer by LPCVD process with 4" quartz tube furnace (Fig. 2.10). Optical microscope picture (left) and Raman spectrum (right).

300-nm thick SiO_2 on silicon wafer. The Raman spectrum in Figure 2.11 clearly shows a 2700-cm^{-1} peak and a 1590-cm^{-1} peak with similar intensity levels. It is good evidence of single layer graphene, and successful low-pressure CVD set-up.

b. DC tests

To measure the emittance of the DFEAs, we have produced new pepperpot anode structures. The pepperpot consists of an array of ~50-μm holes with a pitch of 1 mm laser machined into a 50-μm thick piece of steel shim stock. This shim is spotwelded to the front of an ~600-μm support plate to prevent flexing under the stress of the applied electric field. A steel ring spacer about 3.5 mm long is attached to the support plate with silver paste. Atop the ring spacer is attached a small, high-sensitivity, phosphor screen for imaging the beamlets.

Using this new apparatus, we considered the effects of the double-oxidation process on array performance. Figure 2.12 shows the emission performance for arrays fabricated with 0.5-μm single oxidation with and without 5% N_2, and for arrays fabricated with (0.5 μm, 1 μm) double oxidation with 5% N_2. The thicker final oxidation clearly results in sharper emitters and enhanced emission properties. Perhaps more interesting is the Fowler-Nordheim plot of these data, which is shown in Figure 2.13. The curvature of the 0.5-μm single-oxidation data at low electric field is indicative of a distribution of tip radii. The (0.5-μm, 1-μm) double oxidation data are almost devoid of curvature, which suggests a tighter distribution of tip radii.

Using these pepperpots, we performed emittance measurements of our cathodes. These measurements were made on a 5-μm base, 7-μm pitch cathode that was produced using a (0.5 μm, 1.0 μm) double oxidation. The experimental arrangement is shown schematically in Figure 2.14. The anode-cathode gap was set using 170-μm quartz capillaries, however the actual gap width is only ~100 μm due to the thickness of the pepperpot and the diamond and braze layers. The cathode could not be

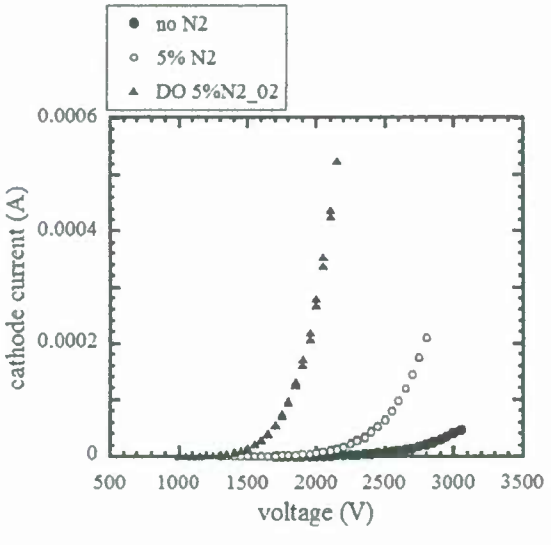

Figure 2.12: Current vs. Voltage data for 0.5-μm single oxidation with and without 5% N_2, and for (0.5 μm, 1 μm) double oxidation with 5% N_2.

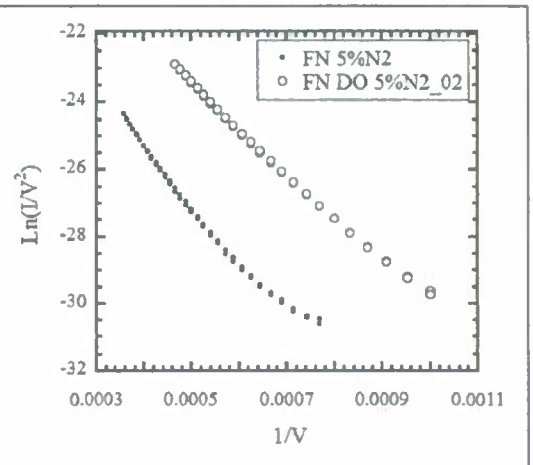

Figure 2.13: FN plot for 0.5-μm single oxidation with 5% N_2, and (0.5 μm, 1.0 μm) double oxidation with 5% N_2. The lack of low-field curvature in the double oxidation data suggests a tighter distribution of tip radii.

conditioned for uniform emission prior to the emittance measurements due to damage suffered by our high-voltage pulser, which is now under repair. Figure 2.15 shows an image of the phosphor screen when the anode voltage was set to 2100 V. The stability and uniformity of the top-right beamlet indicated that a large number of emitters were contributing to the current. A linescan of this beam spot was used to determine the rms divergence, $\sigma_{x'}$, of the beam from the DFEA. Provided that the array is conditioned for uniform emission, the normalized rms transverse emittance can be determined from the formula

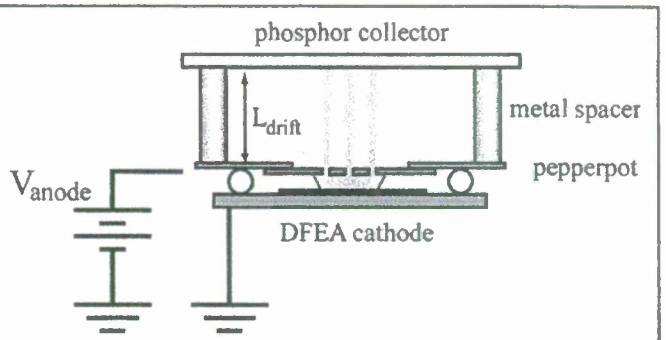

Fig. 2.14: Experimental arrangement for measuring the emittance of electron beams from DFEAs.

$$\varepsilon_N = \frac{1}{2} r_c \beta\gamma\sigma_{x'}$$

where r_c is the radius of the cathode, and β and γ have the usual relativistic meaning. After the divergence has been corrected for the size and defocusing of the pepperpot aperture, we find that the normalized rms transverse emittance for a 1-cm diameter cathode is 9.28 mm-mrad. The other beamlets were clearly the result of a small number of emitters and were not analyzed.

After the pulser was repaired, we demonstrated high-current conditioning using a 10x10, 100-μm pitch array. As demonstrated in the program previously, morphological conditioning of the emitters begins at around 1 μA/tip. A phosphor screen image of the emitted beam is shown in Figure 6. 2.16. These experiments were limited by thermal damage to the anode above each beamlet. The cathode maintained a reasonable level of performance despite the poor vacuum conditions and the liquification and evaporation of the anode immediately above each emitter. It should be noted that thermal conditioning of this cathode gave the same results as those described in the previous section. A Fowler-

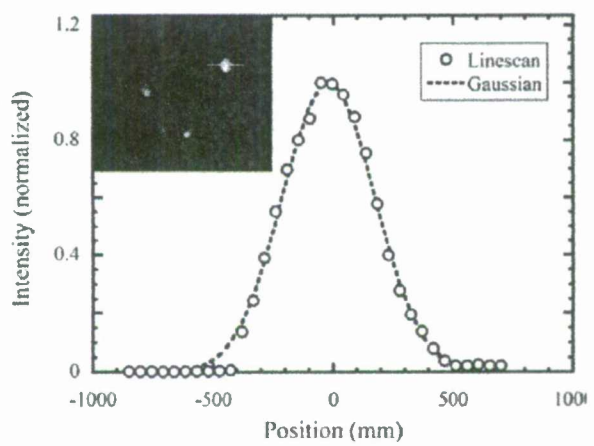

Fig. 2.15: Phosphor screen image of beamlets emerging from the pepperpot anode. The linescan and its Gaussian fit are from the top-right beamlet and are analyzed to find the beam divergence.

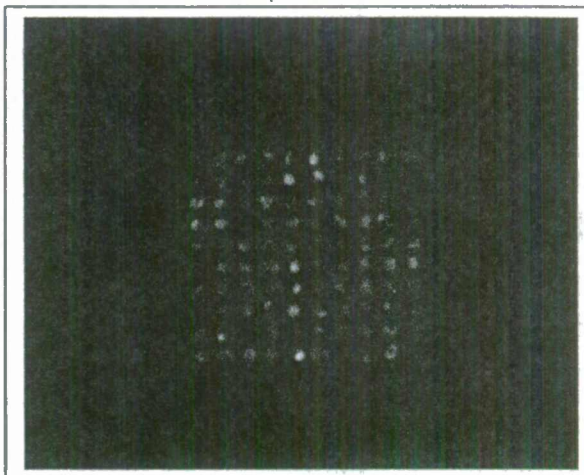

Figure 2.16: Phosphor screen image of the beam emitted by a 10x10 array with 100-μm pitch during operation at ~1 μA/tip; 95/100 tips are emitting at comparable levels

Nordheim plot of the cathode performance before and during thermal conditioning at 430 °C is shown in Figure 2.17.

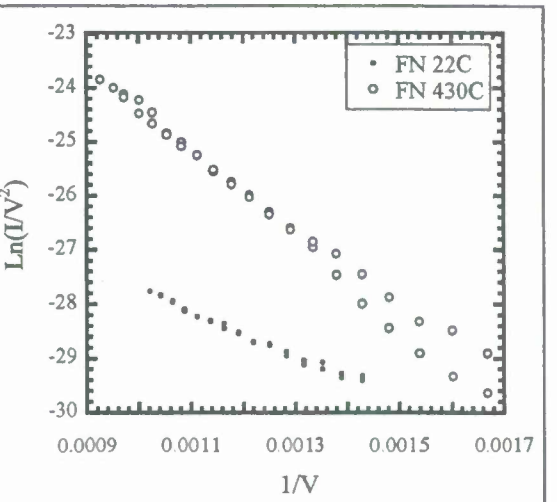

Figure 2.17: Fowler-Nordheim plot of 10x10 array performance before and during thermal conditioning at 430 °C.

To achieve a current density on the order of 30 A/cm^2, roughly the peak value required (assuming a 1-cm cathode) for 1-A average operation of a field emission injector, we require ~5 μA/tip uniformly across a 4-μm pitch dense array. We have previously demonstrated that operation of DFEAs at currents above 1 μA/tip results in excellent uniformity due to thermal assisted field evaporation of the nanotips. This morphological conditioning is self-limiting, ceasing when the modified tip structure is able to support the local joule heating and field stress. At μA/tip current levels, the power density in the beam from a single emitter is enough to cause significant damage to the anode. When testing the arrays in a close-diode configuration the beams from dozens or even hundreds of emitters overlap making the power density at the anode prohibitively large. The resulting back bombardment of anode material on the cathode damages the emitters and limits performance. There are two strategies for avoiding this damage: the use of low-duty-factor, pulsed DC to drive the cathode, or the use of an electron gun that extracts the beam without anode interception and collects it remotely at a sufficiently low power density. For this second approach we have developed a "minigun."

The first version of the minigun is shown in Figure 2.18. We chose to use hardware from Kimball physics for construction due to its modularity. We are able to quickly reconfigure the minigun to meet the requirements of a variety of cathode sizes and operating fields. To gate the emission from the cathode we use an anode plate with an aperture that is typically 0.5-1.0 mm

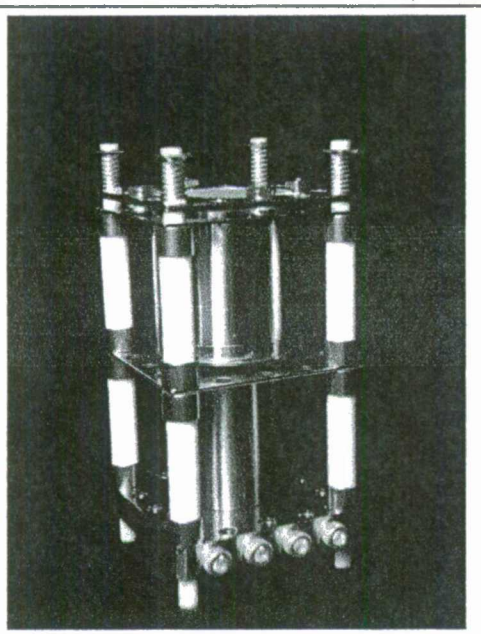

Figure 2.18: Version #1 of the minigun for DFEA testing.

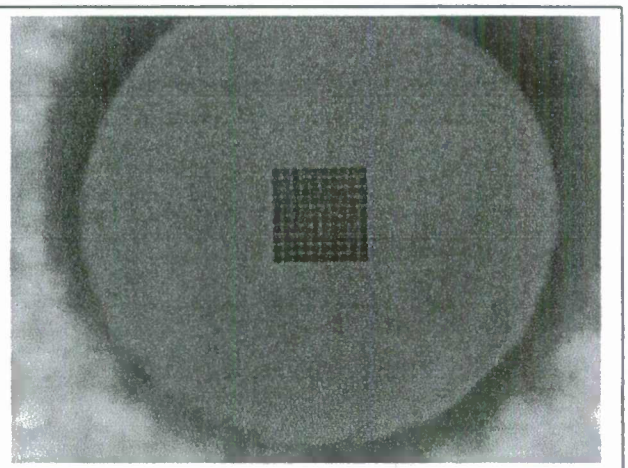

Figure 2.19: Optical microscope image of a 10x10, 20-μm pitch cathode aligned under the 1mm anode aperture of the MG

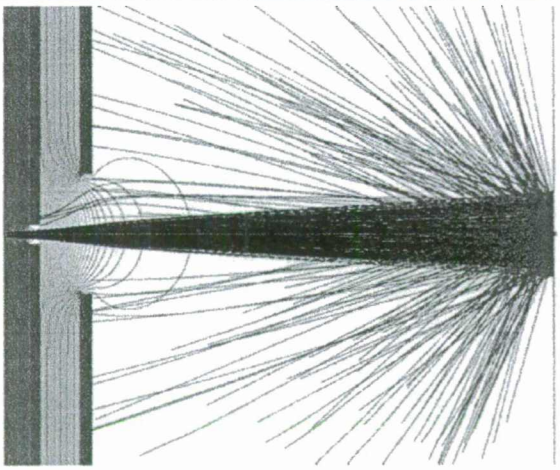

Figure 2.20: SIMION simulation of typical trajectories and equipotentials for version one of the MG.

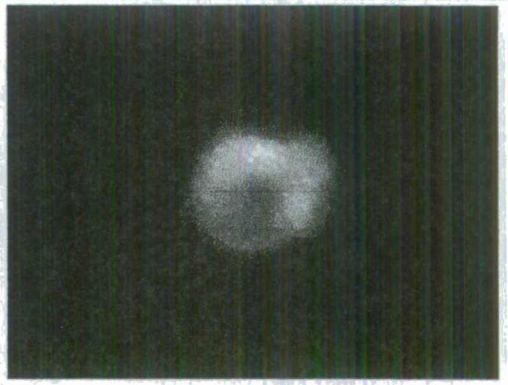

Figure 2.21: ~1 cm beam spot from a 10x10 array in version one of the MG. The dark area is the result of thermal damage, and subsequent charging

in diameter. The cathode is fixed to a tall cylinder to provide extra isolation and aligned beneath the anode aperture. A Faraday cup (FC) with a phosphor screen collector is located immediately after the anode plate. The long drift distance of the FC allows the beam spot to spread out thereby reducing the power density at the anode to safe levels. A microscope image of a 200-μm cathode aligned under a 1-mm anode aperture is shown in Figure 2.19. Figure 2.20 shows a SIMION simulation of typical equipotential contours and electron trajectories for this version of the MG. An example of the measured beamspot is given in Figure 2.21.

There were two primary problems with version #1 of the MG: the spacers that were used to set the distances between electrodes resulted in unacceptable leakage currents at high field, and the P22-B phosphor on ITO glass (Kimball) was significantly damaged during operation. To address these issues we developed the improved MG shown in Figures 2.22 and 2.23. We removed the alumina spacers and switched to clamp-plate assemblies for holding the components. We have run the MG up to 18kV without detecting leakage through the insulators. Elimination of the leakage current allows us to make precise measurements of the amount of field emission current leaving the cathode and arriving at the other electrodes. We also developed a ZnO phosphor on sapphire that has a 30x higher thermal conductivity than the glass based Kimball screens. Additionally, we extended the drift space in the FC substantially to allow for more beam spreading prior to collection.

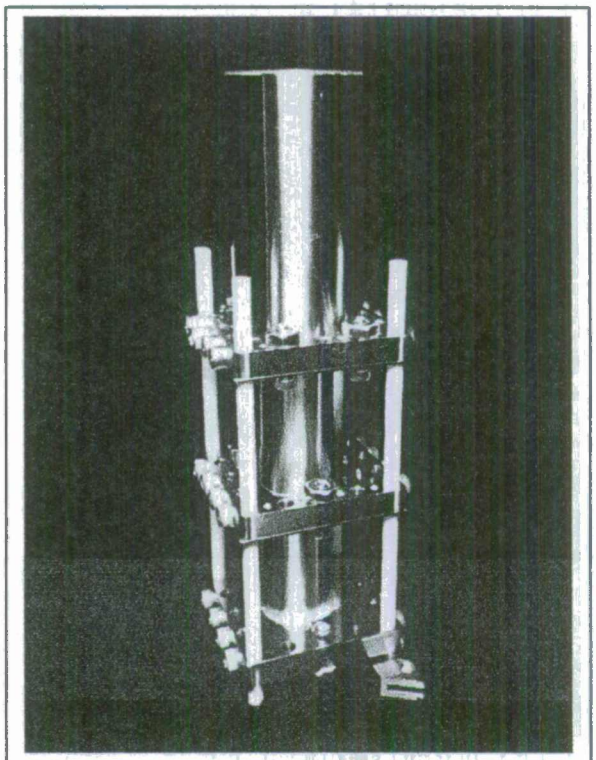

Figure 2.22: Version #2 of the MG using clamp-plate assemblies, a ZnO on Al_2O_3 phosphor screen, and a larger drift distance in the FC.

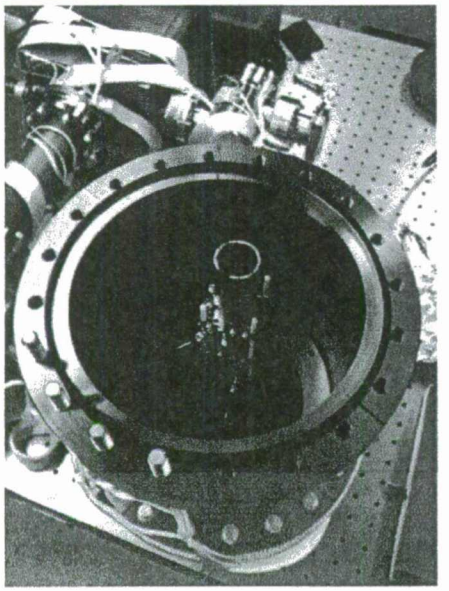

Figure 2.23: Version two of the MG installed and ready for testing in the high vacuum test stand.

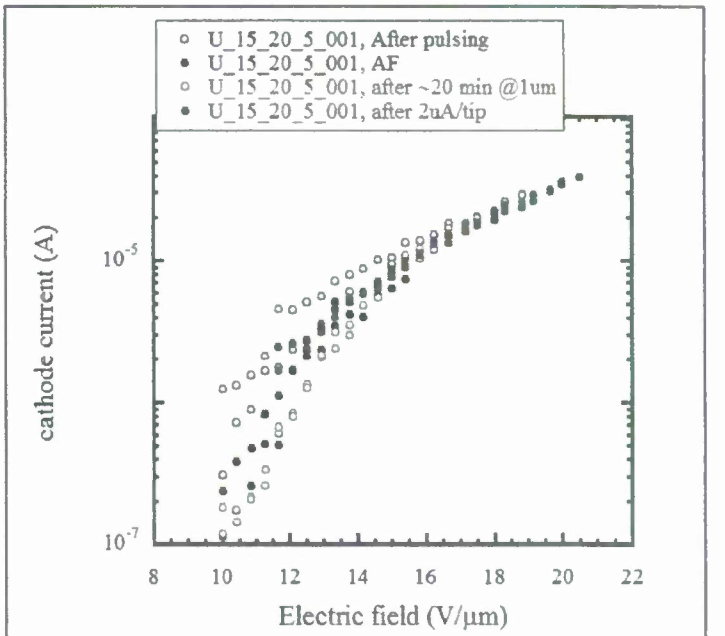

Figure 2.24: IV plot showing cathode performance up to ~1 μA/tip. The required field is rather high due to non-idealities in the lithography of this batch of cathodes.

The first cathode tested in the version two MG was a 5x5, 15-μm base, 20-μm pitch array. The MG cathodes were fabricated using electron beam lithography due to the ease of rapid customization. Unfortunately, the tolerance of the lithography was insufficient and resulted in wedge-like tips with radii on the order of 50 nm. Accordingly, the required field for turn-on and high current operation was very high. All 25 tips were imaged in the scanning electron microscope prior to testing. An IV plot demonstrating the performance of the array up to ~1 μA/tip is shown in Figure 2.24. While the maximum extracted current was ~4 μA/tip, prolonged operation at this level was not possible due to explosive emission from the edge of the cathode's molybdenum substrate. All 25 tips were imaged in the SEM after testing and found to be nearly identical to their pre-testing state. This indicates that significant morphological conditioning did not occur due to the ability of the much larger tip radii to support higher current levels. In the SEM we observed contamination on the cathode confined to the array area (Figure 2.25). X-ray analysis showed that this was likely carbon and not any metals from the steel anode. It is likely that the high current density and moderate vacuum (10^{-6} Torr) resulted in the dissociation and deposition of carbon from organic molecules in the background. This cracking would happen most strongly near the cathode where the beam intensity is maximum. This would explain the small length scale (~50 μm) over which the contamination is confined. It also suggests that the uniformity of this layer, to some degree, is an indirect indicator of the emission uniformity. The uniformity of the beam spot itself, an example of which is given in Figure 2.26, does not reveal the tip-to-tip emission uniformity. This is

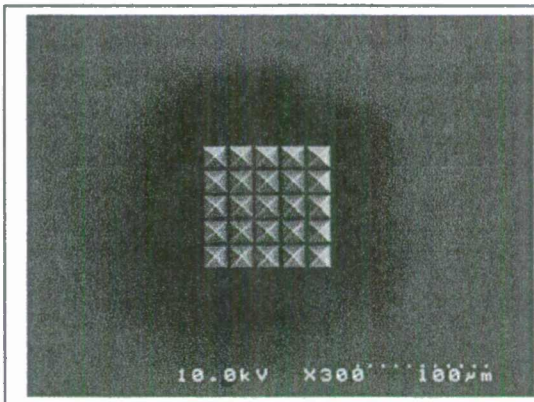

Figure 2.25: SEM image of the cathode after testing at ~4 μA/tip. The dark spot around the cathode was determined to be carbon contamination from the high beam intensity and moderate vacuum.

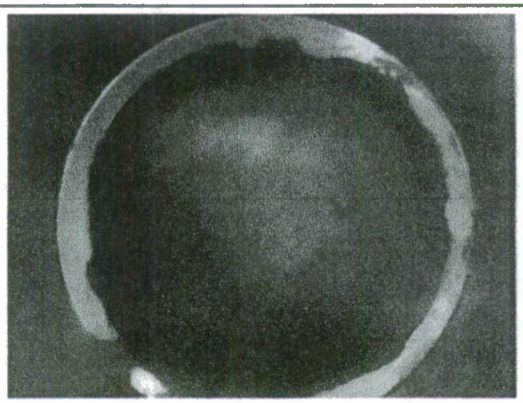

Figure 2.26: Typical beam spot from the 5x5 array at around 2 μA/tip.

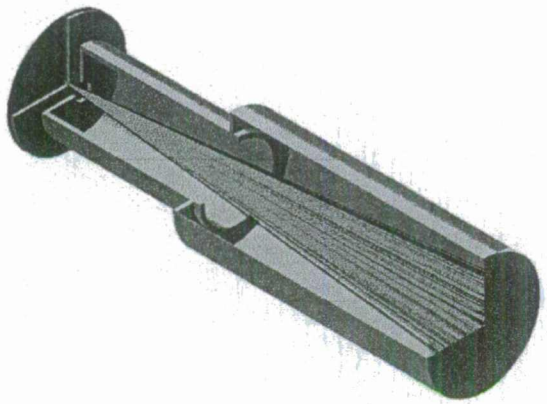

Figure 2.27: SIMION simulation of version two of the MG. The conditions in the simulation are the same as those that produced the beam spot in Figure 2.26.

because the beam from a point source at the cathode spreads to almost the same size as the beam from the entire cathode. This is evident in the SIMION simulation in Figure 2.27 where the green trajectories are from a point source and the black trajectories are from a 100-μm cathode.

c. Surface conditioning and diamond film composition

It is well known that surface hydrogenation of diamond-based electron sources can play a critical role in determining their performance. This is principally due to the negative electron affinity (NEA) of the hydrogenated surface and has been clearly demonstrated by recent experiments involving single crystal diamond amplifier cathodes (DAC) at Brookhaven National Laboratory (BNL). While the emission surface of our polycrystalline, CVD-diamond field emitters is very different from that of the DAC, our previous experiments have demonstrated the importance of the surface condition (e.g. adsorbed contaminants and resonant tunneling) in determining emission behavior. Therefore, we have attempted to determine the effects of hydrogenation on the emission performance of our DFEA cathodes. It should be noted that when the diamond cathodes are grown in our CVD reactor, the plasma is 90% hydrogen. In fact, the growth of diamond is only possible because of the preferential etching of graphitic content by the hydrogen. This means that at every moment in the growth process, the diamond is exposed to hydrogen atoms/ions. Therefore, it seems likely that every diamond grain in the entire structure, both surface and interior, is passivated with hydrogen.

The aforementioned studies at BNL found that hydrogenation of the diamond surface could be accomplished by exposure to atomic hydrogen after first heating to ~800 °C to open up dangling bonds on the surface. While the NEA properties of the surface were lost after exposure to atmosphere, the hydrogenation was stable and the NEA could be fully recovered by heating the diamond to ~450 °C. To investigate the possibility that our diamond is already hydrogenated, we performed the following tests (all heating and measurement performed at ~10^{-7} Torr):

1. Tested the current-voltage (IV) behavior of the cathode in a close-diode arrangement after fabrication and prior to any thermal or high-current conditioning

2. Heated the cathode to ~450 °C for ~1 hour and then checked the IV behavior after cooling to room temperature.

3. Heated the cathode to ~450 °C for ~1 hour and checked the IV behavior (while hot)

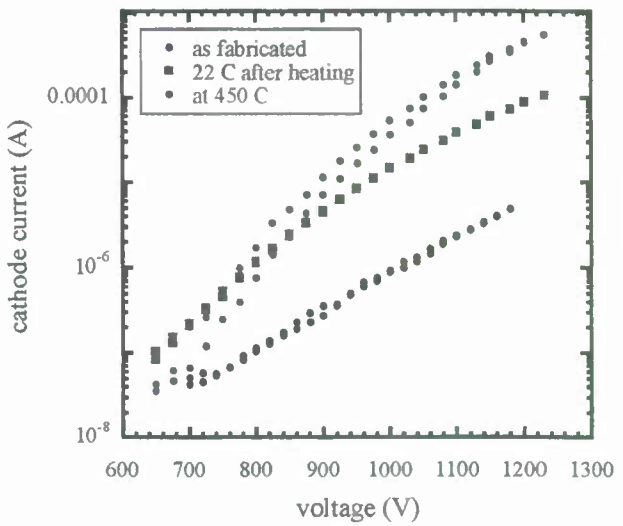

Figure 2.28: Performance for an array of ~10^5 emitters during various stages of thermal conditioning. Black - as fabricated, Blue - after heating to 450 °C and then cooling to 22 °C for 5 hours at 10^{-7} Torr, Red - taken while at 450 °C during a second heating cycle.

The results of these measurements are shown in Figure 2.28. We find that heating the cathode in this manner results in dramatic improvement over the "as-fabricated" IV performance. Allowing the cathode to contaminate at room temperature in either atmosphere or vacuum (~10^{-7} Torr) after the initial heat treatment results in performance that is slightly lower than that for operation at 450°C. This post-heating, room-temperature performance is still more than an order of magnitude improved over the as-fabricated behavior. This suggests that there is detrimental contamination from the fabrication process, possibly from the silicon and oxide etches, that must be removed prior to operation.

Next we investigated rehydrogenation of the cathode surface. We designed and constructed an atomic hydrogen source that consists of an aluminum oxide tube with a tungsten heating coil running down its center. The coil is operated with an input power of ~100 W to achieve temperatures of ~1700°C. Based on existing literature we expect a cracking efficiency of a few percent. The hydrogen source is placed approximately two inches above the cathode surface. The cathode heater and the hydrogen cracker were baked at ~500°C and ~1000°C respectively prior to attempting hydrogenation. The cathode was heated for three hours at 750°C in order to clean the surface and generate dangling bonds for hydrogenation. The hydrogen cracker was increased to full power and the partial pressure of hydrogen was increased to ~ 10^{-5} Torr. After exposure for one hour at 750°C the cathode heater was turned off and the cathode was allowed to cool to ~200°C with the hydrogen source on. Figure 2.29

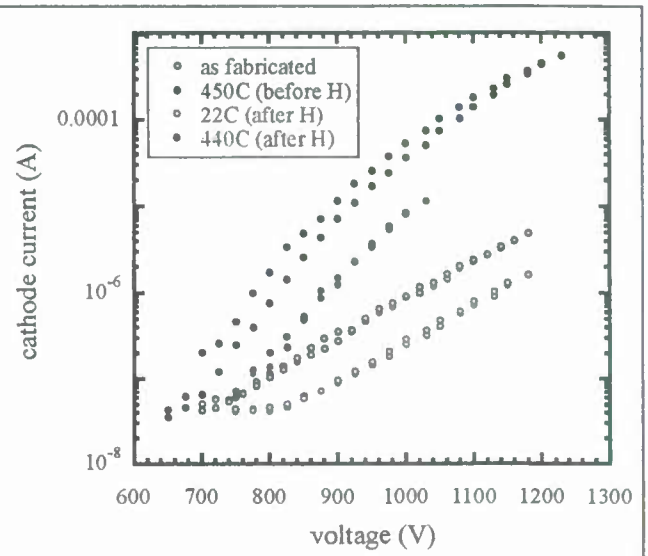

Figure 2.29: IV after attempting hydrogenation compared to as-fabricated and heat treated cathode behavior.

shows the IV performance before and after this conditioning process. While the qualitative behavior is similar, the performance is markedly reduced relative to that for a cathode conditioned with 450°C after fabrication. This could be due to the low cracking efficiency of our source, or perhaps contamination from the relatively poor vacuum level in the chamber.

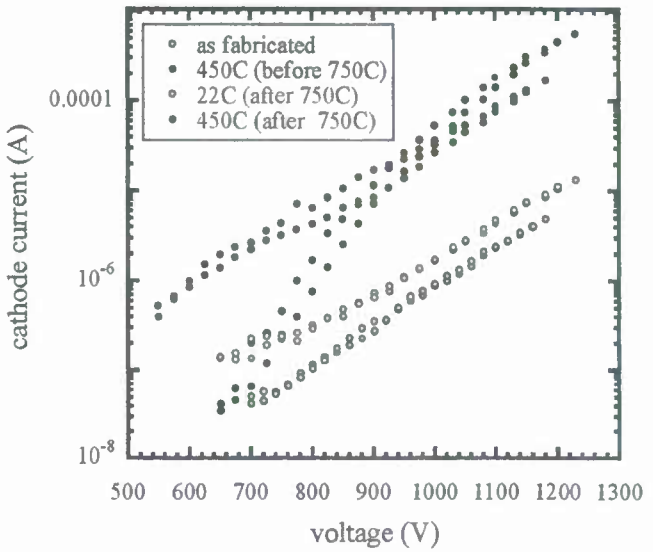

Figure 2.30: Performance for low and high temperature (450 °C) before and after attempting to dehydrogenate for 1 hour at 750 °C. The performance modification is not presently understood.

Finally, we considered the effects of dehydrogenation on the emission performance. To accomplish this, we heated the cathode to 750°C in vacuum (10^{-7} Torr) for ~1 hour in the absence of hydrogen. This should liberate the surface hydrogen and leave the dangling bonds, perhaps to be passivated in some way by residuals in the vacuum. The cathode certainly contains hydrogen due to its growth environment, however, it is not known if this hydrogen is able to act in some way as a reservoir to replenish surface hydrogen when it is removed. After "dehydrogenation" the shape of the IV curves is quite different from that of the heat treated cathode, as seen in Figure 2.30. The significant deviation of the dehydrogenated curves at low field is not understood. It is a positive result that a simple, low-temperature treatment of the as fabricated cathode results in the best observed performance thus far.

We also investigated the conductivity of our

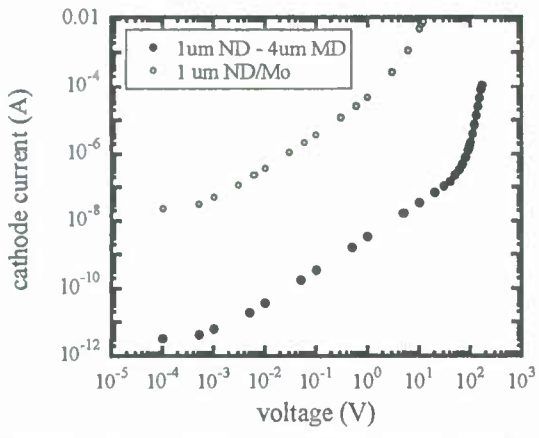

Figure 2.31: Current vs. voltage using a single probe on the surface of an array made with 1 μm ND and one made with 1 μm ND and 4 μm MD.

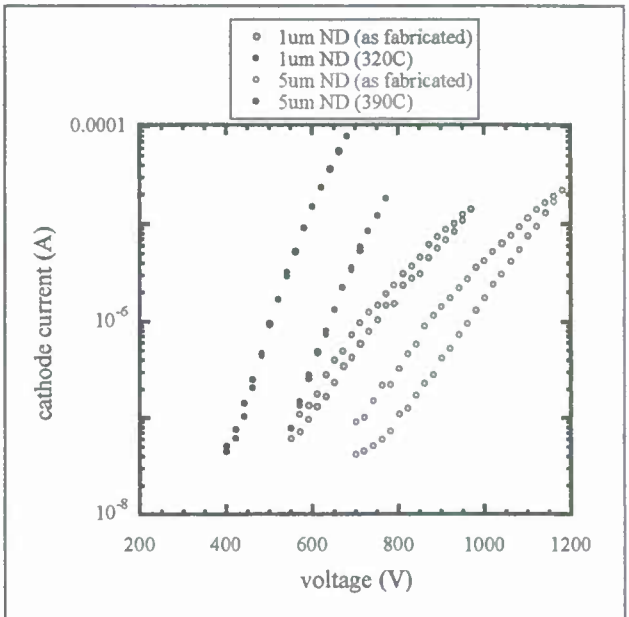

Figure 2.32: IV behavior for two cathodes, one with 1 μm of ND and one with 5 μm of ND. The thin ND cathode outperforms the thick ND cathode by a factor of ~50 for the same applied electric field.

diamond films using a simple single-probe technique. The results of these measurements for two cathode types (1 μm of nanodiamond (ND) on molybdenum, and 1 μm of ND on 4 μm of microdiamond (MD)) are shown in Figure 2.31. The conductivity of both films is very low until high fields (>10 V/μm) where it becomes nonlinear. To investigate the effects of film composition on emission performance we fabricated two morphologically similar arrays, one with 1 μm of ND and one with 5 μm of ND. Both films were brazed directly to molybdenum substrates without any microdiamond or metal back-filling. The cathodes were thermally conditioned and tested in the usual way. The results are shown in Figure 2.32. The IV behavior is qualitatively similar for both cathodes but the thin ND cathode is found to outperform the thick ND cathode by a factor of ~50 for the same applied electric field. This suggests that minor changes in composition or structure can result in dramatic improvements in emission performance.

d. RF tests

It was not possible to do RF testing of an ungated cathode at LANL or NPS since these guns were not available. However, an ungated cathode was delivered to Fermilab for testing in their HBESL injector. These tests were performed by Philippe Piot as part of a DARPA program. The following description is taken from an internal report provided by Dr. Piot (private communication).

The geometry of the FEA cathode used for the experiments reported below appears in Fig. 2.33. It consists of pyramidal diamond tips with their extremities separated by 10 μm. The typical pyramid base is ~ 1.5 μm and the radius of curvature of the tip is on the order of 10 nm. The FEA pattern was formed on a Molybdenum substrate via a lithographic process. The Molybdenum substrate was subsequently brazed on a cathode holder made of Molybdenum and compatible with the load-lock insertion mechanism used in the RF gun; see Fig. 2.34. The cathode holder was inserted in the RF gun and its position was adjusted to insure the gun resonant frequency remains at 1.3 GHz (as monitored with a spectrum analyzer). To insure electrical contact between the cathode holder and RF gun cavity walls, a Cu-Be spring is used; see Fig. 2.34 (b). This spring was also found to be source of spurious field emission.

The FEA cathode was located on the back plate of a 1.3-GHz 1.5-cell RF gun operating on the TM_{010} π mode powered by a 3-MW klystron. As shown

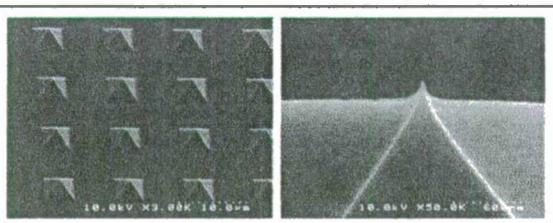

(a) (b)

Figure 2.33: Electron-microscope photographs of the FEA pattern (a) and close up of one pyramidal tip (b). The scales are respectively 10 and 0.6 μm for photographs (a) and (b).

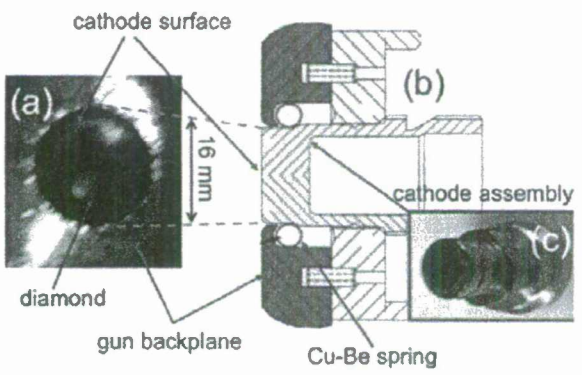

Figure 2.34: Overview of the FEA cathode assembly. Photograph of the FEA cathode in its final position in the RF gun (a), section schematics of the cathode assembly inserted in the RF gun (b), and photograph of the cathode holder with diamond coating on its font surface (c).

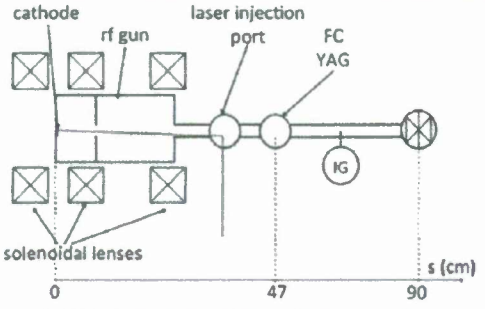

Figure 2.35: Experimental setup used to carry field-emission studies. The legend is as follows: "FC": Faraday cup, "IG" ion gauge, "YAG": scintillating screen for transverse beam density measurement.

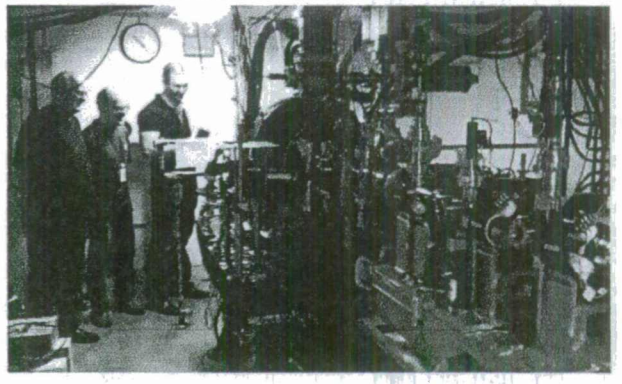

Figure 2.36: The A0 gun and beamline at the Fermilab HBESL facility used for the rf tests.

in Figures 2.35 and 2.36, the RF gun is surrounded by three solenoidal lenses that control the beam's transverse size.

The charge and transverse distribution of the emitted electron beam can be measured with respectively a Faraday cup and scintillating screen; see Fig. 2.35. Both diagnostics are located at $z = 0.47$ m from the cathode and are remotely insertable. An ion gauge located 0.5 m from the gun monitored the vacuum level in the section composed of the gun and diagnostics. Typical vacuum levels in the area are $\sim 1\times10^{-9}$ Torr.

The first series of measurements consisted of characterizing the "background" field emission from the Cu-Be spring. For these studies a standard phtotocathode – a Molybdenum cathode holder coated with Cs and Te layers – was used. We found only small emission (current over a 40-μs pulse was ≤ 0.5 μA). In this process the beam distribution at X1 was monitored and an image of the currents of the solenoidal lenses were tuned to image the cathode on X1. The measured patterns are displayed in Fig. 2.37 (a) and (b) for two cathode peak electric fields. As expected a petal-like pattern appears and is a signature of the spring coils field emission. Similar measurements carried for the FEA cathode appear in Fig. 2.37 (c) and (d). In contrast to the CsTe measurement, a strong emission from a localized area is observed. At low E-field this emission seems localized to a small area of the diamond pattern while as the field increases the emission seems to arise from a larger area consistent with the diamond array size. These measurements were performed with a 40-μs rf macropulse.

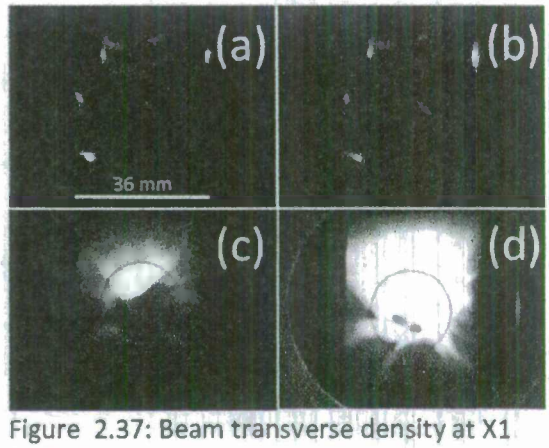

Figure 2.37: Beam transverse density at X1 for CsTe (a)-(b) and FEA (c)-(d) cathodes. Distributions (a), (c) are obtained for a cathode peak field amplitude $E_z \simeq 20.5$ MV/m while (c), (d) correspond to $E_z \simeq 23.6$ MV/m

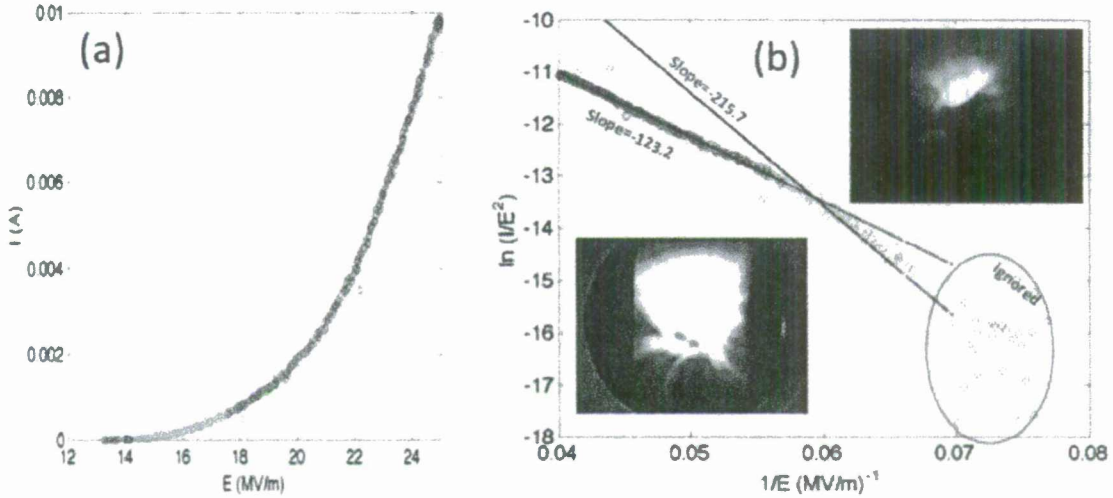

Figure 2.38: Beam transverse density at X1 for CsTe (a)-(b) and FEA (c)-(d) cathodes. Distributions (a), (c) are obtained for a cathode peak field amplitude $E_z \simeq 20.5$ MV/m while (c), (d) correspond to $E_z \simeq 23.6$ MV/m

During the running period, the vacuum level was monitored and did not appreciably deteriorate, remaining at $\leq 1.2\times10^{-9}$ Torr.

The current was also collected for long period of time (typically up to one to two hours); see Figures 2.39 and 2.40. The apparent current drift may be traced back to klystron power drift with time. Accounting for the E-field drift and computing an "Instantaneous" FN slope as $S \equiv E \times \ln(I/E^2)$ indicates that the emission is stable with typical relative variation $\frac{\Delta S}{\langle S \rangle} \simeq \pm 2$ %; see Figures 2.39 and 2.40 (right plots).

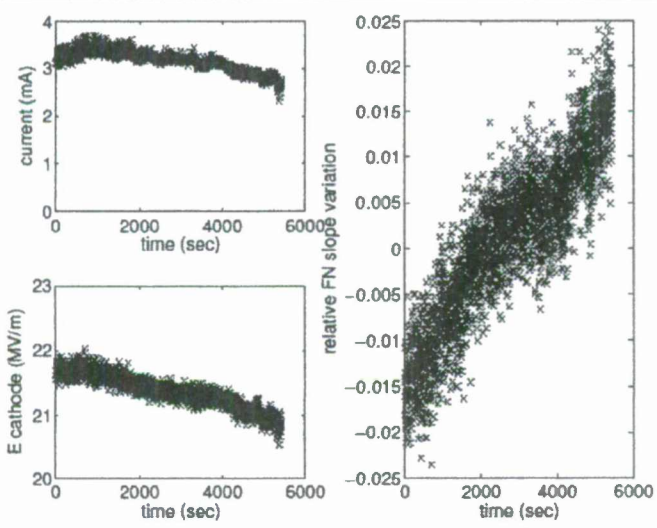

Figure 2.39: Long-term stability studies for $\hat{E} = 21.7$ MV/m: evolution of the beam current (top left), the cathode applied field (bottom left) and the normalized change in the Fowler-Nordheim slope (right) as a function of time.

Several experiments are planned for a second experimental run. For this run, the photocathode drive laser will be available, following repairs. We will withdraw the cathode slightly from the cavity to better shield the edges of the cathode from the high accelerating fields. This may reduce the spurious emission from the edges of the cathode and from the spring. We will do further measurements of the Fowler-Nordheim

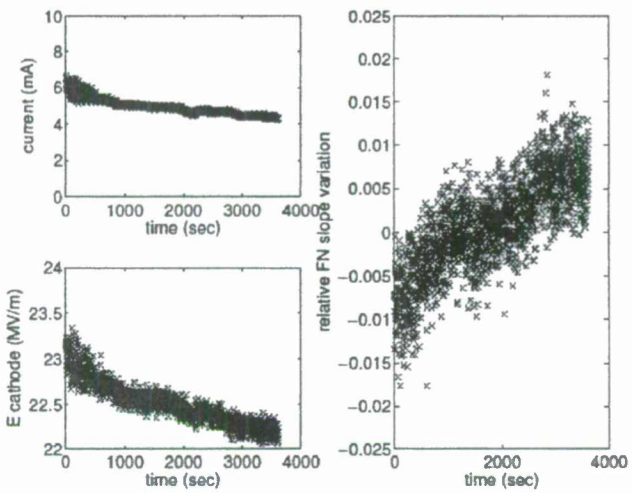

Figure 2.40: Long-term stability studies for $\hat{E} = 23$ MV/m: evolution of the beam current (top left), the cathode applied field (bottom left) and the normalized change in the Fowler-Nordheim slope (right) as a function of time.

behavior of the cathode and examine the transverse distribution of the emitted current to see if it is correlated with the total current. Finally, we will do experiments on photo-field emission using the cathode drive laser. This is a possible means for controlling the emission timing.

3. Gated arrays

a. Simulations of gated emitters

Under a separately funded DARPA program, we have simulated the performance of a single gated emitter and acceleration of the beam in an RF gun and linac. An example is shown in Figure 3.1. The

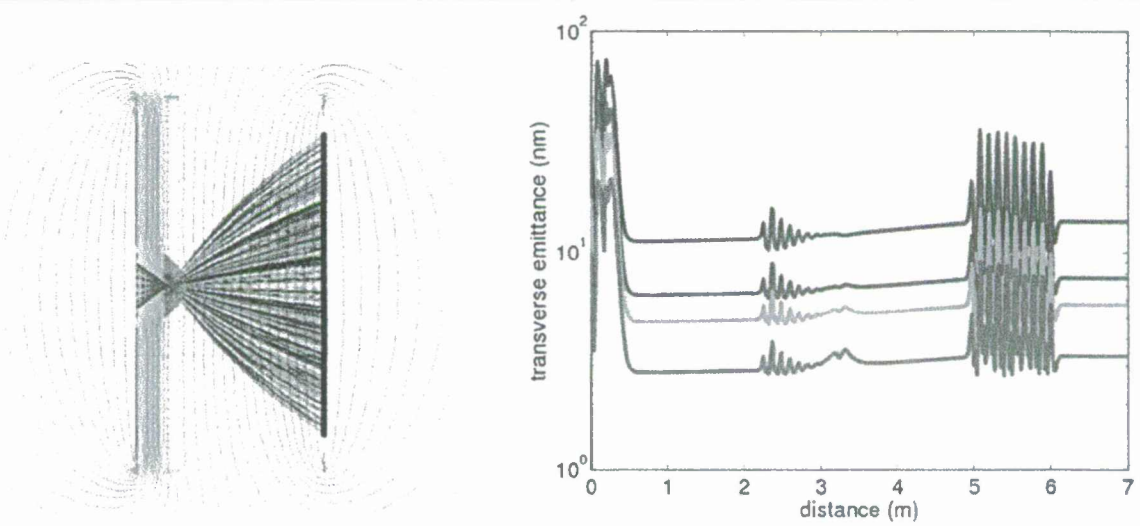

Figure 3.1. Simulation of a single gated emitter (left) and acceleration to 30 MeV (right). The simulations shown on the right were done by Daniel Mihalcea, of Fermilab, with DARPA support (private communication).

DARPA program requires a beam of exquisitely small emittance at low average current, on the order of 200 nA. This can be achieved with a single gated emitter. The emittance at the cathode is 2 nm, and the emittance after acceleration to 30 MeV is 4 nm. Although the emittance and current from an array are much larger than those from a single tip, the simulations are of direct relevance to the JTO program.

b. Fabrication of gated arrays

With the shift of fabrication to the VINSE facility, it became possible to develop the "volcano" process for fabricating gated emitters. The conventional volcano process may be applied to any ungated device in three simple steps. First a layer of SiO_2 ranging in thickness from 1-2 μm is deposited on the array surface. The accumulation of SiO_2 occurs more rapidly at sharp features such as the edges and the tip, resulting in a bulbous cap on the top of the pyramid. Next a 100-200 nm layer of niobium is deposited on the array. The bulbous areas of quartz shadow certain parts of the pyramid surface, preventing the accumulation of niobium in these regions. The process is completed by using an oxide etch to attack these exposed areas and remove the bulbous cap, thereby exposing the emitter tip. Sharp edges on the pyramid tend to prevent efficient shadowing by the cap and result in a low yield for the process. This may be overcome by rounding the edges using double oxidation or other techniques. An example of a completed gated emitter is shown in Figure 3.2.

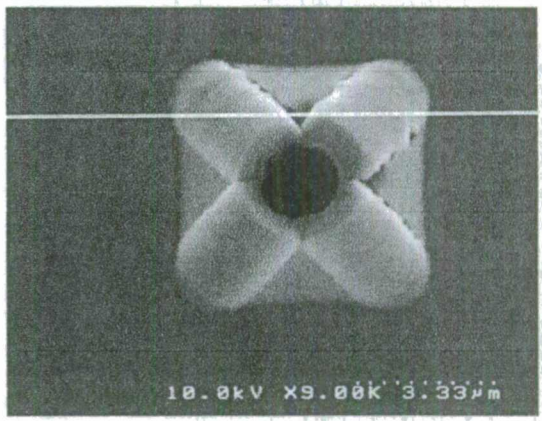

Figure 3.2: Example of a gated emitter produced by the conventional volcano process.

There are two problems for the conventional volcano process (evaporation of gate insulator and gate electrode sequentially): the integrity of the evaporated quartz, and sharp edges of the pyramid. The sharpness of side edges prohibits selective etching at volcano cap opening step. For this reason, we decided to change the gate insulator. Considering process margins and performance of the final device, the thermal SiO_2 is one of the promising materials for the gate insulator. We therefore use thermal SiO_2 from the mold formation as the gate insulator with preserving technique during mold removal step. Changing etchant for mold removal from KOH to Ethylenediamine base solution can save the thermal SiO_2 owing to etch selectivity to silicon. An important benefit of recycling mold SiO_2 is the adhesion and conformity of the gate insulator to the shape of the FEA. A potential risk of the reuse of mold SiO_2 is possible defects in the insulator generated during MPECVD process.

We selectively expose only the region near the tip apex since saving the thermal SiO_2 in other areas is necessary for the volcano process. We spin PMMA 950 4% on preserved mold SiO_2 with 3000 rpm. A low-power oxygen plasma etching is done on the coated PMMA (descum process) without any patterning effort. In order to verify opening the PMMA only in vicinity of the apex, we performed a buffered oxide etch on entire structure. Fig. 3.3 clearly shows exposed diamond emitter apex, and buffered oxide etching time can control the exposed volume of apex.

Figure 3.4 shows a result of the volcano process on preserved mold SiO_2 followed by selective exposure of the tip apex. Unexpectedly, we suffered bad opening probability during lift-off etching after

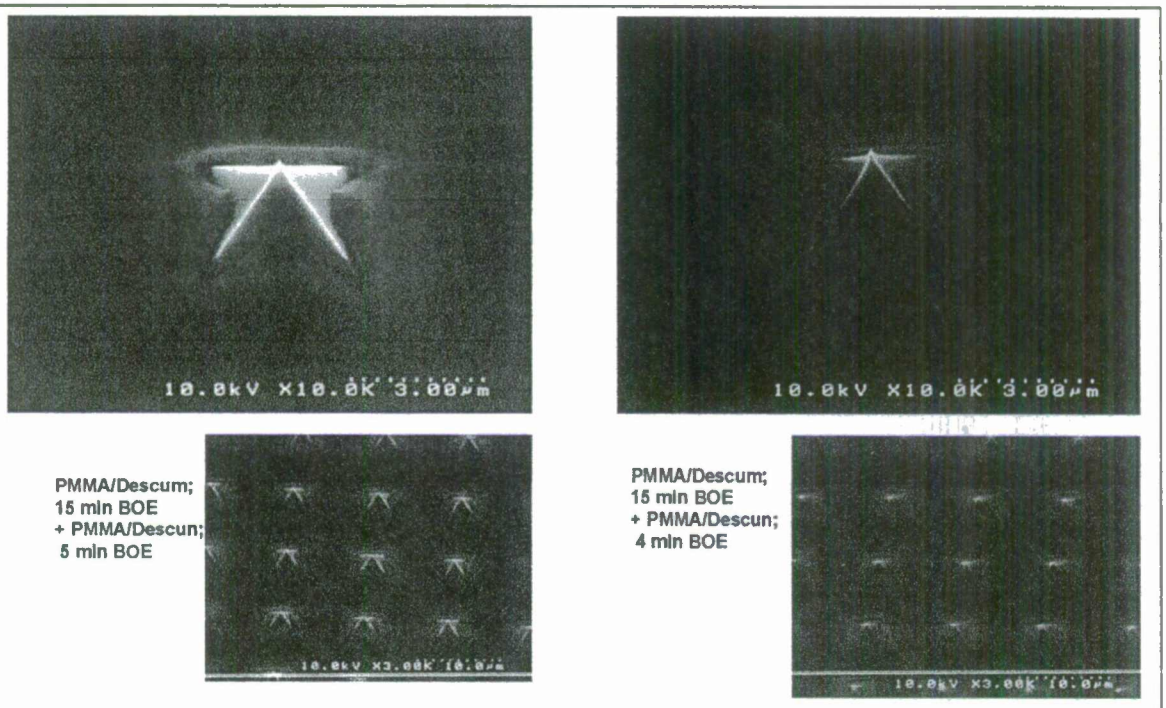

Figure 3.3: Examples of selective exposure of tip apex in preserved mold SiO_2. Left and right pictures are applied double spun PMMA/descum process but different etching times.

evaporations. We also suffered from bad adhesion between mold SiO_2 and evaporated SiO_2. The low opening yields can be improved by more sharpening apex, but bad adhesion will be critical issue for the performance of final device.

Figure 3.5 depicts the new process flow for gated structure using the preserved mold SiO_2. This approach is quite different from the conventional volcano process, which uses the shadow of a formed quartz ball on the apex as the attack point of the wet etchant. We will use a simple isotropic etching technique on spin-coated photoresist film. During the spin coating process, we expect selective thinning in vicinity of apex compared to flat areas. The subsequent isotropic oxygen plasma etch exposes the area near the apex of FEA beforehand. The feasibility of this step is shown in Figure 3.3. The conventional reactive ion etching with CF_4 gas etches Nb and SiO_2 with remaining photoresist as an etch masking layer. Even though the etch selectivity of CF_4 among Nb, SiO_2, and photoresist is known to be poor, the thickness difference of those films can provide enough margin to achieve the final structure.

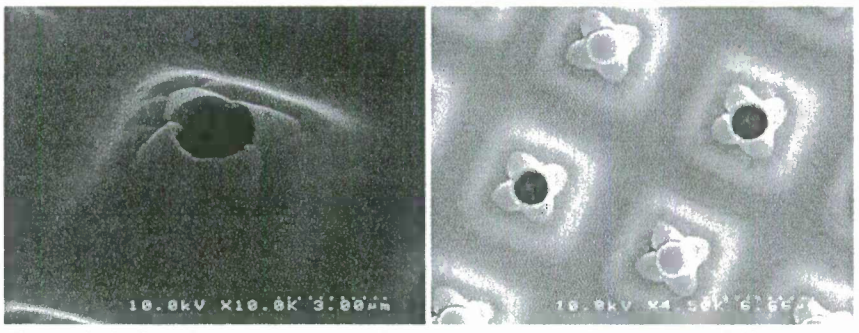

Figure 3.4: Resultant structure of volcano process (evaporated SiO_2 and Nb gate electrode on top of the structure on the right).

The idea of preserving the mold SiO_2 and using it as gate insulator requires optimization of the brazing process. We suffered from self-

delaminating of the interface between CVD diamond and mold SiO_2 layers. The solution was to maintain a thermal gradient across the structure – to keep the Si mold cooler than the brazing alloy. This could be achieved by either thermal radiation from the brazing assembly on a vacuum hot plate or by keeping the temperature of the Si mold low in a plasma system. We used a microwave plasma CVD system (MPCVD) for the latter approach. We set the substrate heater of the MPCVD at 650 C and attached the Si mold to it. We controlled the hydrogen plasma to heat the Mo disk effectively above the brazing temperature, and succeeded to braze without self-delaminating the Si mold.

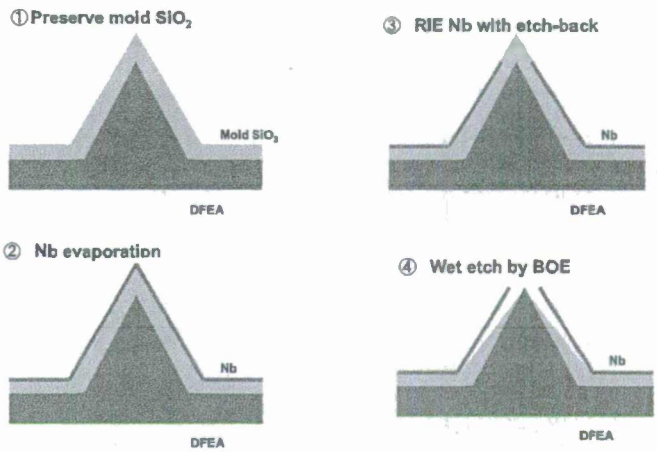

Figure 3.5: Proposed fabrication procedure for gated structure. Niobium is the first choice for gate electrode and thermally grown SiO_2 will be the gate insulator.

We also found that the thickness of the mold SiO_2 is a critical parameter. During etching of the mold silicon, the residual stress between the mold oxide and the silicon can be released, and it can cause large-scale catastrophic damage to the diamond tips. From our observations, the thickness of the mold oxide should be less than 1.8 μm.

in the volcano process, the Nb gate is applied to the entire cathode structure, and then the Nb is removed from the region around the tips. A reactive-ion-etching recipe for Nb uses CF_4 gas and additive O_2 gas. The role of O_2 is to enhance etch selectivity to the SiO_2 layer, and also O_2 plasma can etch the photoresist. Since the photoresist is thinnest near the tips, the Nb is removed there, exposing the tip. The O_2 content in the reaction gas is essential in this application. We tried CF_4 40 sccm and O_2 5 sccm at 75 mTorr chamber pressure with 140 W RiE power only. The equipment model is the Phantom II made by Trion, and VINSE modified the system with an inductively coupled plasma module. The system uses DC bias on the substrate holder as a parameter to match the impedance during plasma generation, and the DC bias was from -40V to -200V under the specific recipe. Figure 3.6 shows the result of this recipe for 10 minutes on a 20 μm-base dense DFEA with 3 times 2000-rpm spin coating of AZ5214E photoresist. The RIE recipe could establish a volcano structure, but the roughness of the etched Nb layer was too large for a gate electrode, as shown in Figure 3.6. The roughness is mostly caused by excessive damage to the photoresist under reactive plasma with DC bias.

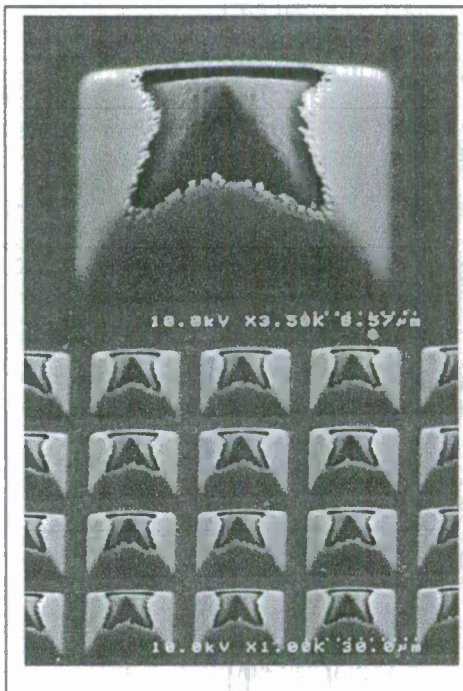

Figure 3.6: SEM pictures of RiE applied result (tiited images with different magnifications). Photoresist film was removed, and SiO_2 was not completely removed.

in order to smooth the roughness of the etched Nb layer, we tried to use the inductively coupled plasma (ICP) mechanism installed on the same Phantom II system. The recipe was ICP power 500 W with 40 sccm CF_4 and 5 sccm O_2 at 30 mTorr chamber pressure. Figure 3.7 shows the result of the ICP recipe. The new recipe smoothed the roughness of the Nb layer by hardening the photoresist with hot (500 W) plasma and reducing mechanical attack on the photoresist due to less DC bias. The actual amount of DC bias cannot be monitored without RIE power due to the configuration of the equipment. In Figure 3.7, the Nb layer under the partially transparent photoresist showed smoother edges than in Figure 3.6. This was followed by wet etch of the SiO_2 layer to expose the sharp diamond cathode tip. The total plasma etch time was 5 minutes, and the wet oxide etch time was 20 minutes.

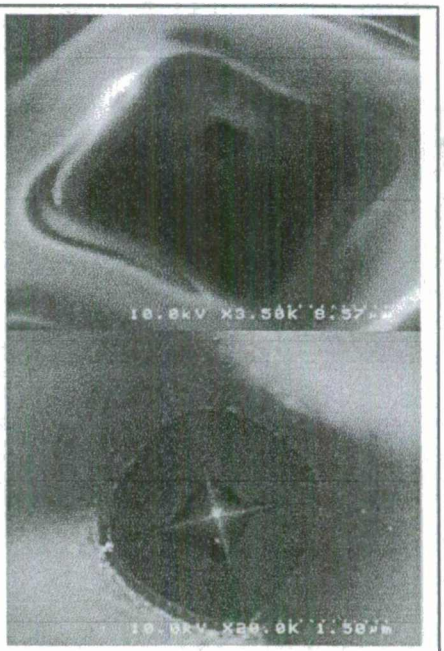

Figure 3.7: SEM pictures of ICP RIE applied result: tilted image (top); detail top view (bottom). Photoresist film is still covered on the gated structure.

We found that simple solvents could not remove the photoresist after it was hardened by the reactive plasma. Niobium has several oxide forms (NbO, NbO_2, and Nb_2O_5), and removing the hardened films by oxygen plasma may alter the property of Nb electrode. Hence, it was necessary to find a method to remove the photoresist without aggressive oxidation. UV exposure followed by solvent treatment is the solution. A flood exposure under a mask aligner breaks the polymer chains in the hardened photoresist and reduces the molecular weight of the polymer. This increases the dissolution rate in acetone. Figure 3.7 shows the cleaned gated structure on a 5-μm base DFEA.

Under a separate (DARPA) program we have developed an alternative method for opening the gates of a gated field-emitter array. In this approach, the gates are opened individually by focused-ion-beam milling. The method yields more controlled opening of the tips, but is suitable only for small arrays.

The FIB system we use has a Ga liquid as the ion source, and 30-kV maximum accelerating voltage. Initially, we cut a circle, as shown in Figure 3.9. However, some damage to the tips occurred during the oxide etch, caused by the cap falling on the tip during the etch step. Subsequently, we have had better success milling the entire cap over the tip by raster-scanning the focused ion beam over the area to be

Figure 3.8: After photoresist removal by UV flood exposure and solvent cleaning: top view (left); tilted view (right). The volcano structure was established on a 5-μm base DFEA

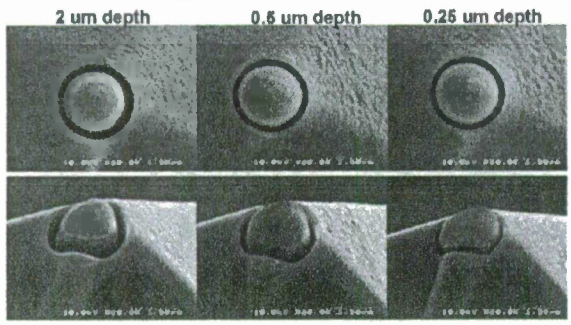

Figure 3.9: FIB milling of gate opening.

Figure 3.10: Gated cathode formed by milling the entire gate cap over the tip.

exposed. A typical result is shown in Figure 3.10.

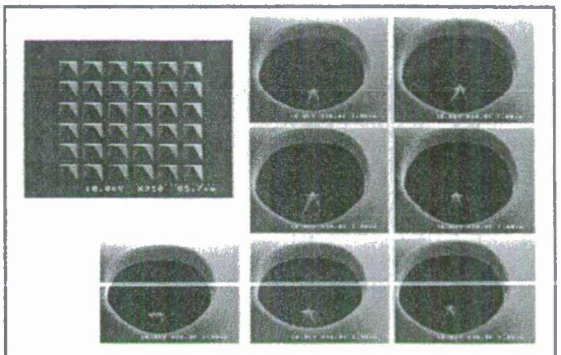

Figure 3.11. Tips formed by 3-pass e-beam lithography.

Another problem that we experienced was the formation of double tips, especially on pyramids with larger bases. This is believed to be caused by angular misalignment between the square pattern being lithographed and the crystal axes of the silicon. Several methods were explored to address this. In one approach, the mask was defocused on the resist to make the edges "fuzzy." The best results were obtained by e-beam lithography in which the mold is patterned with circles instead of squares. The anisotropic etch still produces square pyramids, but the orientation is now irrelevant. By using multiple passes of the e-beam to lithograph the sample, good circles were obtained, which produced higher yields of perfect tips, as illustrated in Figure 3.11.

c. DC tests

We test emission from volcano arrays using the test arrangement shown in Figure 3.12. The cathode in the test chamber is a 6x6 array of pyramids with diamond tips and a metal gate over the pyramids with a small opening to allow the electrons to escape. In this case, we determined the gate was too small and the diamond emitter too recessed to allow many electrons to exit through the hole in the gate. That is, there was a very strong cathode-to-gate current and a much smaller cathode-to-anode current.

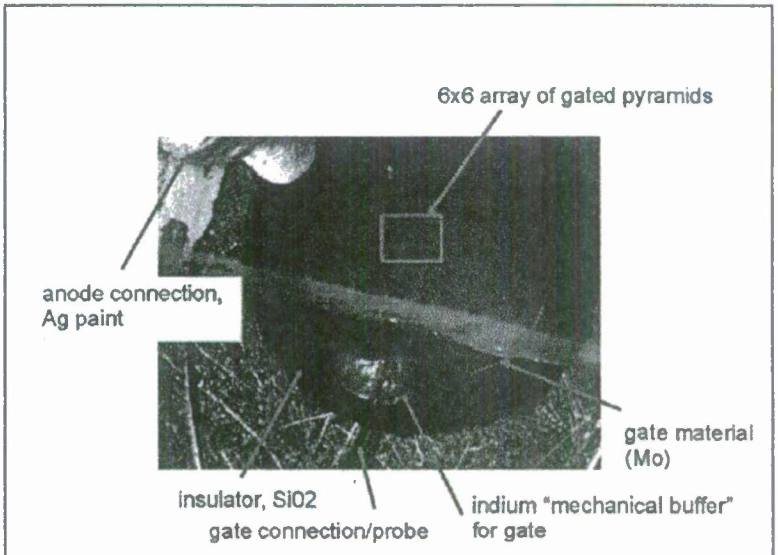

Figure 3.12. Photograph of a gated array in the test chamber.

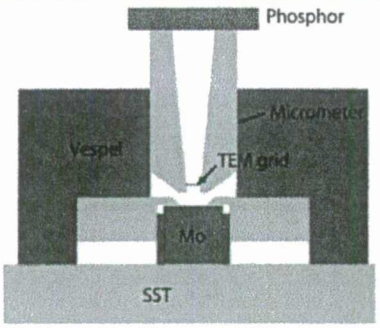

Figure 3.13. Schematic diagram of small cathode test apparatus.

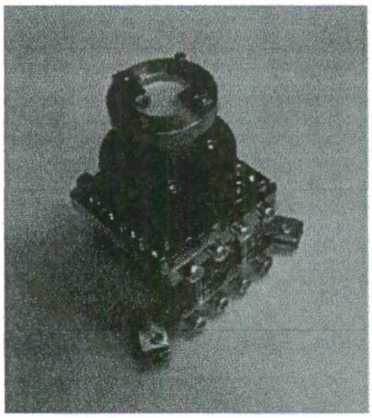

Figure 3.14. Photograph of small cathode test apparatus.

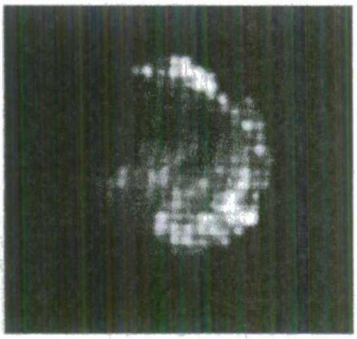

Figure 3.15. Image of electron beam on phosphor, showing shadow of TEM grid.

We test the individual emitters formed by the FIB milling process in a new apparatus, shown in Figures 3.13 and 3.14, that measures the voltage-current behavior of the cathode and images the beam on a phosphor screen. A typical image of the beam showing the shadow of the 500-mesh TEM grid is shown in Figure 3.15. By comparing these data to simulations, we will optimize the parameters such as gate aperture and pyramid size.

In order to center the emitting tip on the cathode, we fabricate an array of pyramids, braze it to the substrate, and then open just the tip closest to the center of the substrate. We have encountered unexpected failures at the buried tips, as shown in Figure 3.16. The damage seems to be caused by the anode field, rather than the gate field. If necessary, we will avoid this problem by fabricating only a single, open tip and carefully aligning it at the center of the cathode in the brazing step. No problems are observed at the open tip, as shown in Figure 3.17.

d. RF tests

Under a separate DARPA program, a gated cathode will be tested first at Niowave, Inc., in a 700-MHz gun and then at Fermilab in the HBESL injector. The cathode holder with coaxial gate feed is shown in Figures 3.18 and 3.19. It was designed to be compatible with the guns at Fermilab, and was fabricated, and delivered by Niowave, Inc. We have

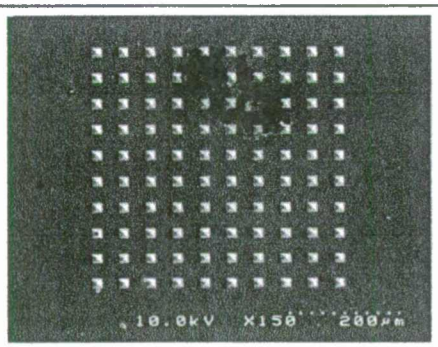

Figure 3.16. Damage to cathode at sites of buried tips.

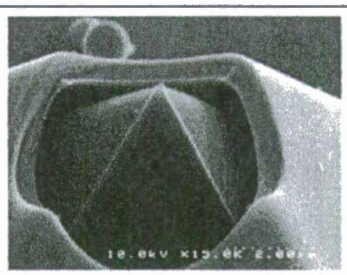

Figure 3.17. Open tip (third from bottom in left-most column of Figure 6) is undamaged.

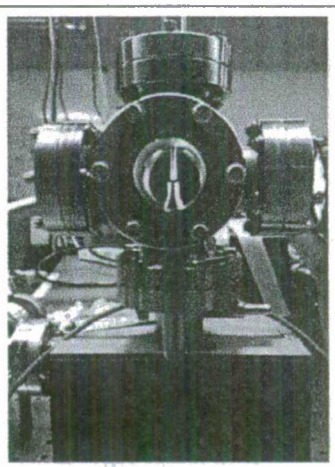

Figure 3.18. Cathode holder developed by Niowave, shown in test stand for rf measurements.

measured the rf properties of this cathode holder, and we will begin tests with a DC anode field and RF gate bias when an optimized emitter design has been developed in the small apparatus described above. The small apparatus mimics the design of the Niowave holder, and provides faster turn-around as well as more detailed data on the beam properties.

Figure 3.9. Cathode holder for gated cathodes with coaxial feed.

---

i C. A. Brau, "Quantum-degenerate beams from carbon nanotubes," unpublished.
ii G. R. Neal, *Phys. Rev. Lett.* **84**, 662 (2000).
iii P. G. O'Shea, private communication.
iv C. A. Spindt, IEEE Trans.Electron. Dev **38**, 2355 (1991).
v P. R. Schwoebel, C. A. Spindt, and C. E. Holland, J. Vac. Sci. Technol. B **23**(2), 691 (2005).
vi S. C. Leemann, A. Streun, and A. F. Wrulich, Phys. Rev. ST-AB **10**, 071302 (2007).
vii P. R. Schwoebel, C. A. Spindt, and C. E. Holland, J. Vac. Sci. Technol. B **23**(2), 691 (2005).
viii W.-P. Kang, J. L. Davidson, M. Howell, B. Bhuva, D. L. Kinser, Q. Li, and J.-F. Xu, Vacuum Microelectronics Conference, 1995. IVMC, pp. 287-291, 30 July – 3 August 1995
ix W.-P. Kang, J. L. Davidson, M. Howell, B. Bhuva, D. L. Kinser, D. V. Kerns, Q. Li, and J.-F. Xu, J. Vac. Sci. Tech. B, **14**, 2068 (1996)
x J. D. Jarvis, H. L. Andrews, C. A. Brau, B. K. Choi, J. L. Davidson, W.-P. Kang, and Y.-M. Wong, J. Vac. Sci. B **27**, 2264 (2009).
xi J. D. Jarvis, H. L. Andrews, C. A. Brau, B. K. Choi, J. L. Davidson, Ivanov, W.-P. Kang, C. L. Stewart, and Y.-M. Wong, "Pulsed Uniformity Conditioning and Emittance Measurements of Diamond Field-Emitter Arrays," Proceedings of the 31st International Free Electron Laser Conference, Liverpool, United Kingdom, August 23- 28, 2009.
xii J. W. Lewellen, Phys. Rev. ST-AB **8**, 033502 (2005).